

AD-A080 372

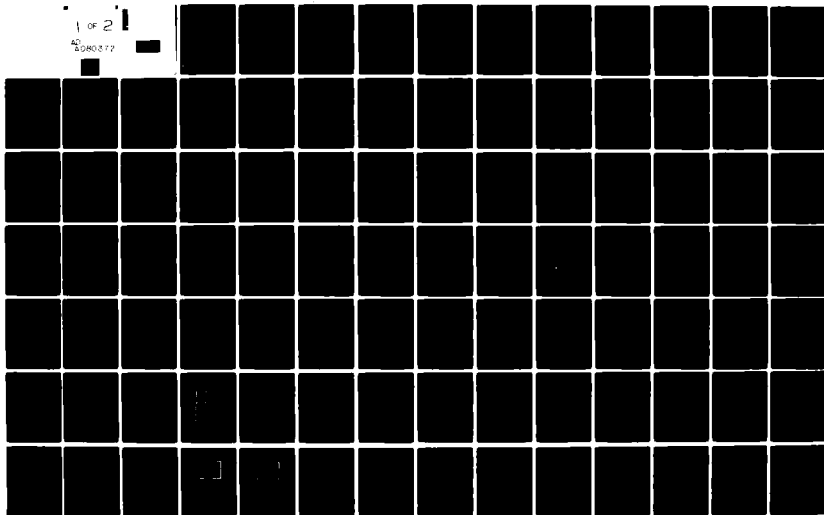
AIR FORCE INST OF TECH WRIGHT-PATTERSON AFB OH SCHOO--ETC F/6 28/3
ROTATION RATE SENSING VIA MAGNETOSTATIC SURFACE WAVE PROPAGATIO--ETC(U)
DEC 79 R J POTURALSKI
AFIT/6E/EE/79-28

UNCLASSIFIED

NL

1 OF 2

AD-A080 372



6
ROTATION RATE SENSING
VIA MAGNETOSTATIC SURFACE WAVE
PROPAGATION ON A THICK YIG RING.

9 Master's THESIS,

14 HFIT/GE/EE/79-28;

10 Richard J. Poturalski
Captain USAF

11 3 Dec 79

12 4

Approved for public release, distribution unlimited

012 225

WAVE PROPAGATION ON A THICK YIG RING

THESIS

Presented to the Faculty of the School of Engineering
of the Air Force Institute of Technology

Air University (ATC)

In Partial Fulfillment of the

Requirements for the Degree

Master of Science

by

Richard J. Poturalski
Captain USAF

Graduate Electrical Engineering
3 December 1979

Accession
NIMS
DIC 100
Unrecovered
JAN 1968
FBI
A

Preface

In December, 1974, Newburgh, Budreau, Blacksmith, and Sethares of the Air Force Cambridge Research Laboratories (AFCRL), New Bedford, Massachusetts, proposed a technique using magnetostatic surface waves to measure relative, non-inertial rotation rates. Subsequent to the 1974 proposal, Sethares experimentally and theoretically profiled surface wave propagation on a simple ring geometry using a thin yttrium-iron-garnet (YIG) film as a propagation medium.

In February, 1979, I was introduced to the proposed AFCRL scheme by my thesis advisor, Major Salvatore R. Balsamo, professor of electrical engineering at the Air Force Institute of Technology. It was my assigned task to advance the AFCRL research by investigating the use and performance of a thick, single crystal YIG ring as a practical rotation rate sensor. This thesis is the result of that investigation.

Because of the complexities of any original research, I am deeply indebted to those individuals who supported me throughout this effort. Specifically, I would like to thank my thesis committee, Major Balsamo and Professors R. S. Potter and (Captain) J. M. Borky,

for their technical guidance throughout my research. I am equally indebted to Mr. James C. Sethares for his participation in the significant amount of theoretical analysis this unexplored topic required. I also want to thank Mr. Jim Adair and Mr. Mark Calcatore of the Air Force Avionics Lab for use of their facilities, equipment, and talent. And, I especially want to thank my wife, Naoma, for her secretarial and, most importantly, moral support.

Contents

Preface	ii
List of Figures	vi
List of Tables	viii
Abstract.	ix
I. Introduction	1
Background	1
Statement of the Problem.	4
Plan of Attack.	4
Sequence of Presentation.	5
II. Magnetostatic Theory.	7
Phenomonological Model.	7
Magnetostatic Modes	13
Experimental Observations	18
MSSWs on a YIG Ring	20
III. Magnetostatic Rotation Rate Sensing	23
General Concept	23
Phase Sensitive Sensor.	24
Frequency Sensitive Sensor.	26
MSSW Relations.	30
IV. MSSW Rotation Rate Sensor Design.	35
General Design Aspects.	35
RF Probe Design	39
Rate Sensor Design Factors.	42
V. Experimental Results.	52
General	52
System Losses	55

	MSSW Parameter Identification . . .	59
	40 Experimental Results	67
	4f Experimental Results	72
	Analysis of Corruptive Effects. .	76
	Experimental Summary.	79
VI.	Conclusions	80
	Summary	80
	Reccomendations	81
	Bibliography.	83
	Appendix A: Symbols and Abbreviations	85
	Appendix B: Equipment	87
	Vita.	92

List of Figures

Figure		Page
1	Single Spin System	9
2	Damon and Eshbach Theoretical Slab and Boundary Conditions	15
3	General Dispersion Curve for MSSWs	17
4	Brundle and Freedman Experiment.	17
5	MSSW Propagation Direction, \hat{k} , Relative to H_a and h_{rf}	19
6	Basic Group Delay Experiment Used by Sethares	21
7	Simplified Phase Sensor.	24
8	Simplified Frequency Sensor.	27
9	Cross-sectional View of MSSW Ring Configuration	38
10	Cross-sectional View of RF Probe	42
11	Block Diagram of Phase Sensitive Sensor.	43
12	Block Diagram of Frequency Sensitive Sensor	45
13	Group Delay Set-Up	47
14	Loss Measurement Set-Up.	49
15	System Losses versus Frequency	58
16	Group Delay Sequence	60
17	Group Delay versus Frequency	61
18	Comparative Dispersion Plots	66

Figure		Page
19	Sequence of Phase Patterns at Different Rotation Rates70
20	Phase Patterns as Influenced by Coupling Distance71
21	Comb Oscillator Spectrum72
22	Rotational Effects on MSSW Ring Oscillator Frequency74
23	MSSW Ring Oscillator Spectral Noise. . .	.75
24	YIG Disc Set-Up to Observe Anisotropic Effects.78
25	RF Probe and Ring Assembly90
26	RF Probe and Mount91
27	Thin Film Disc Mount91

List of Tables

Table	Page
I Thick YIG Ring Specifications.36
II Theoretical Dispersion Values for Thick Ring ($H_e = 300$ Oe.).50
III MSSW Experimental Set-Up Parameters and Ranges.53
IV MSSW System Losses57
V Measured and Calculated MSSW Parameters for θ_2 Position62
VI Measured and Calculated MSSW Parameters for θ_1 Position63

Abstract

✓ This thesis presents a theoretical and experimental analysis of the potential use of magnetostatic surface waves to sense non-inertial rotation in a body-fixed reference frame. The analysis primarily focused on the use of high purity, single crystal yttrium-iron-garnet (YIG) as a propagation medium in a thick (0.13 cm.) ring geometry.

The results of several experiments showed that despite the observation of satisfactory surface waves, the lower order wave numbers imposed by the thick ring geometry prevented the achieving of satisfactory rate sensing sensitivity. Additionally, non-uniform behavior as a function of lattice orientation with respect to the surface wave launch site had been observed. It is concluded that this is the result of anisotropic variations which are inherent in the yttrium-iron-garnet medium.

✓

I. Introduction

Background

In 1960, Damon and Eshbach theoretically characterized the existence of two distinct magnetostatic modes on a ferromagnetic slab. With the assumption of proper boundary conditions, their analysis indicated that these modes were unique, frequency dependent solutions to Maxwell's equations and the equation of motion of the slab magnetization. In essence, they concluded that as frequency increases beyond the spin wave region, the magnetostatic behavior changes from one which is distributed across the volume of the slab to one which is strictly a surface mode. In this latter mode, the energy is concentrated at the slab surface along which propagation takes place. The propagation direction is orthogonal to an applied DC magnetic field. The surface wave propagation is initiated by an external RF magnetic excitation (Ref 4).

In further examining the Damon and Eshbach theory, it is seen that the surface wave mode is further characterized as non-reciprocal and dispersive. The mode is non-reciprocal because propagation for a given RF excitation and biasing field is confined to only one

direction. The surface wave is dispersive because the wave velocity increases as the frequency within the surface wave mode is increased. (Hence, the dispersion of the surface wave is termed "positive.")

Later, in 1968, Brundle and Freedman experimentally excited the magnetostatic surface wave (MSSW) mode on a thin, single crystal, YIG slab where the wavelengths of the surface waves were much smaller than the slab dimensions (Ref 4). Their results closely followed the theoretical mode behavior predicted by Damon and Eshbach. In terms of the Damon and Eshbach dispersion relation (Ref 4:133), the correlation between the experimental results and the predicting theory was very good.

In terms of modern avionics, the theory provided by Damon and Eshbach and the experimental analysis performed by Brundle and Freedman, as well as the work contributed by many others, have resulted in many innovative signal processing applications. For example, MSSW technology has been applied to practical tunable microwave oscillators (Ref 8) and variable delay lines (Ref 1) operating within the microwave frequency spectrum. A further extension of this technology was proposed by Newburgh, Blacksmith, Budreau, and Sethares of the Air Force Cambridge Research Laboratories in 1974 (Ref 8).

The AFCRL proposal suggested that MSSW propagation may allow the development of a small, highly sensitive and lightweight non-inertial rotation rate sensor. The sensor would consist of a rotating YIG ring upon which magnetostatic surface waves would be excited. Sensing of the ring rotation rate would be achieved by measuring MSSW phase (or fringe) shifts using an interferometric sensing scheme. Furthermore, in 1974, Sethares showed that MSSW propagation could be achieved on a thin YIG film ring with gallium-gadolinium-garnet (GGG) used as the ring substrate (Ref 10). Results from Sethares' experiment, however, were inconclusive in terms of evaluating the usefulness of the thin film ring as part of a rotation rate sensing system. This resulted from non-uniform behavior of the surface wave as the ring was rotated. Sethares attributed the non-uniformity to the gross "facetting" of the YIG film which occurred during the liquid phase epitaxy crystal growth process. It was subsequently suggested that the thin film disfiguration problem could be avoided by machining the desired ring geometry out of a single crystal YIG boule. Later such a ring was produced, but the YIG thickness was over one hundred times greater than the YIG film thickness. Although the new thick

ring was available at the time of this work, no thorough evaluation of the thick ring in terms of magnetostatic behavior or rotation rate sensing suitability had been performed.

Statement of the Problem

Until this time, no further research into the MSSW rotation rate sensor had been conducted to assess the practical value of MSSW propagation when applied to rotation rate sensing. In order to make such an assessment, the following questions were addressed. First, is it possible to reliably excite uniform MSSW propagation on a ferromagnetic medium when the medium itself is rotating? Second, considering the problems encountered by Sethares with the thin film ring, how well suited is the thick ring to MSSW propagation and, ultimately, sensor sensitivity? Third, what corruptive effects exist and how can they be reduced? And, fourth, does the MSSW sensor provide any practical advantages that would make it a better choice over current rate sensing schemes?

Plan of Attack

This thesis concerns itself with extending the application of MSSW theory to the case of rotation rate sensing with a thick ring. The approach taken is to design and build two different rotation rate sensing

schemes. In one, an experiment is constructed to measure MSSW phase shift in a modified interferometer scheme. In the second, the MSSW YIG ring is adapted to a microwave oscillator system where the shift in oscillator frequency due to rotation of the ring is of interest.

For both applications, it was necessary to accomplish two prerequisite tasks. First, a probe coupling scheme to excite surface waves on the rotating ring had to be developed. Two probes capable of generating and then detecting the surface waves were required. Also, these probes must be able to provide maximum probe-to-probe isolation to restrict unwanted interference between the MSSW signal and the excitation RF field. Secondly, a method of characterizing the thick ring MSSW behavior had to be determined in terms of the actual dispersive character of the wave propagation. This knowledge was needed to form a basis for analyzing the ring performance in the rotating case.

Sequence of Presentation

The existing magnetostatic theory as developed for slab geometries and, later, the ring geometry will be discussed first. This will be followed by a discussion of MSSW propagation when applied to the task of sensing rotation rates. Next, the development and design of two

sensing schemes will be addressed including the description of a means to identify the actual MSSW character of the thick ring. Subsequently, the experimental results will be presented which will be followed by a discussion of the conclusions drawn from this study.

II. Magnetostatic Theory

Phenomenological Model

Magnetostatic behavior in ferromagnetic materials such as yttrium-iron-garnet (YIG) can be explained by describing the interactions between internal magnetic moments as influenced by externally applied magnetic fields. The external fields of interest are periodic time-varying fields, such as RF excitations, and time-invariant, DC fields. Both types are important in explaining magnetostatic effects.

Magnetostatic behavior is classically explained, for example in Sparks (Ref 14) and Kittel (Ref 6), in terms of magnetic moments due to electron spins within a crystal lattice. Here, the spin locations relate to ion sites within the lattice structure where each spin has a magnetic moment associated with it. Due to interactions between neighboring spins in ferromagnetic materials, neighboring spins and their magnetic moments tend to be aligned parallel to one another. The simple summation or, in the macro sense, integration of these magnetic moments over the total sample volume yields a total magnetic moment which can be influenced by external magnetic fields.

When this analysis is expanded to the perturbed case where an external DC field is applied, the nature of this spin system changes. As may be intuitively suspected from a simple field interaction analysis, an externally applied field will alter the discrete spins and, consequently, the total magnetic moment of the ferromagnetic sample.

This can be shown by first considering a simple system with a single spin. As shown in Figure 1, the spin is aligned relative to some fixed reference frame in the normal, unperturbed state. With the application of an external DC field, a torque is produced which results in a precession of the magnetic moment about its equilibrium position. This precession occurs at a fixed precession rate (sometimes referred to as the Larmor frequency) and at some precession angle. Both effects are related to the strength of the applied field where this functional relationship can be expressed as (Refs 14:5 and 5:263-265)

$$\omega = \gamma H \quad (1)$$

where γ is the gyromagnetic ratio. This ratio is a function of the angular momentum and magnetic moment of the spin system (Ref 16:17). It has been fur-

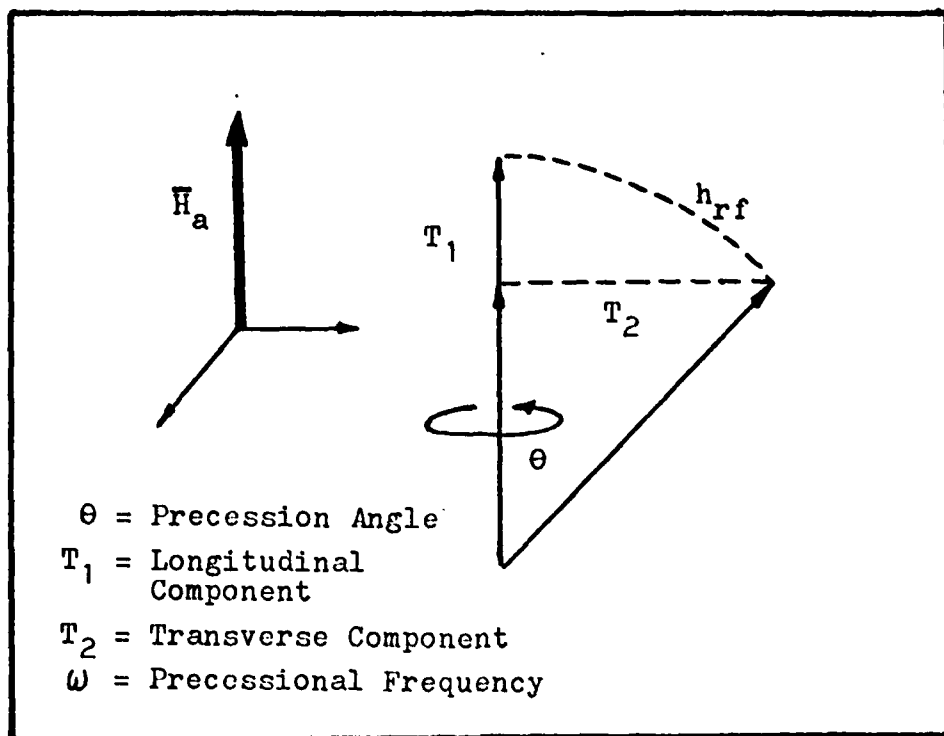


Figure 1. Single Spin System

ther explained by Sparks that if an RF field is directed orthoganal to the applied DC field and set to the same frequency as the precessional rate of the spin system, then there will be a two-fold change in the magnetic moment vector. First, the application of the RF field increases the magnitude of the magnetic moment vector. Second, the RF field will tend to open the precession angle. These effects are pictorially shown in Figure 1.

as the transverse and longitudinal magnetization components of the perturbed spin system.

If this simple case is expanded to one where neighboring spins are introduced, the behavior of the system under the aforementioned conditions becomes further complicated. As the spin system is subjected to an external DC field, the resulting disturbance is opposed by a reactionary field that tends to demagnetize the applied field. This demagnetization, H_d , is a function of the material geometry through the demagnetization factor, N_d , and the saturation magnetization, $4\pi M_s$, of the ferromagnetic material (Ref 13:55). This effect can be simply expressed as a linear function where

$$H_d = 4\pi M_s N_d \quad (2)$$

The net effective field, H_e , that determines the precessional resonance frequency then becomes

$$\bar{H}_e = \bar{H}_a - \bar{H}_d \quad (3)$$

where \bar{H}_a = the applied DC field.

Furthermore, by observing that the RF field, h_{rf} , exerts a torque on the spin system, the equation of

... of the system ... in ...
... of the ...
... of the ...
... of the ...

Discussion

... of the ...
... of the ...
... of the ...
... of the ...

... of the ...
... of the ...
... of the ...
... of the ...
... of the ...
... of the ...
... of the ...
... of the ...
... of the ...
... of the ...

As seen in Figure 1, application of the RF field tends to result in a longitudinal and transverse change in the magnetization moment of the system. When the RF

motion of the magnetization of the system can be expressed as a function of the cross-product, $\vec{M} \times \vec{H}$, where \vec{M} represents the net internal field. As related to the equation of motion of the magnetization by the gyromagnetic ratio, γ , this yields (Ref 14:49)

$$\dot{\vec{M}} = \gamma (\vec{M} \times \vec{H}) \quad (4)$$

Additional complications can be added to the model that further affect the magnetostatic behavior of the ferromagnetic material. For example, nothing has been said about temperature effects, ionic impurities, lattice dislocations, and surface effects.

Theoretically, a pure ferromagnetic material would have, according to the previous discussion, a single discrete precession resonance frequency corresponding to a given value of the net effective field, H_0 . This is not the case in the real world since unavoidable crystalline imperfections have a distinct effect on the precessional change in the spin system as well as anisotropic effects which are difficult to model (Ref 13:52).

As seen in Figure 1, application of the RF field tends to result in a longitudinal and transverse change in the magnetization moment of the system. When the RF

excitation is removed, the system collapses to its normal state. It is theorized that the collapsing is a two-step decay process (Ref 13:31). Two time constants are associated with the collapse: T_1 which affects the longitudinal component and T_2 which affects the transverse component. Further analysis shows that T_1 is primarily due to neighboring spin interactions while T_2 can be attributed to lattice imperfections. The net result is that the precessional resonance condition can occur over a broader range of H_0 than at a single field value. This range, ΔH , is then a measure of the quality of the ferromagnetic material and is most often referred to as the linewidth of the material.

It is of interest to this thesis to point out that pure YIG has an excellent linewidth which is normally much less than one Oersted (Ref 5:300). It is for this reason that YIG is a model specimen for studying magnetostatic behavior. Because of its interior purity, it is interesting to note that ultimately it is the surface quality of a YIG specimen that determines its linewidth. Consequently, the polishing process determines the size and distribution of surface pits on the specimen and the final linewidth.

In addition to crystal quality and surface pits,

other factors enter into the modeling problem. Temperature effects can be very large. For YIG, the saturation magnetization is 1750 gauss with a temperature coefficient of -4.4 gauss per degree centigrade (Ref 16). Anisotropic field effects, although normally small in YIG must also be accounted for. In fact, there is no complete model that describes all the behavioral variations in a ferromagnetic material. However, notwithstanding these limitations, the work done by Damon and Eshbach, Brundle and Freedman, and others has resulted in fairly good models for at least two types of magnetostatic modes.

Magnetostatic Modes

The preceding phenomenological description of magnetostatic behavior remains incomplete, since it does not yet fully describe the allowable behavior modes. Experimentally, many modes have been observed; however, only two general modes have been well modelled. These are the volume and surface modes.

In 1960, Damon and Eshbach developed solutions to Maxwell's equations and the equation of motion of the magnetization for a ferromagnetic slab as shown in Figure 2 (Ref 4). Since magnetostatic behavior in a non-conductive ferromagnetic material is characterized by negligible \vec{E} field component, Maxwell's equations in

the magnetostatic limit become

$$\nabla \times \vec{H} = 0 \quad (5)$$

$$\nabla \cdot \vec{B} = 0 \quad (6)$$

$$\text{where } \vec{B} = \vec{H} + 4\pi\vec{M}_s$$

$$\vec{H} = \vec{H}_e + \vec{H}_{rf}$$

$$\vec{H}_e = \vec{H}_a - \vec{H}_d$$

As illustrated in Figure 2, the conditions placed on the boundaries of the slab are that the normal \vec{B} component and tangential \vec{H} component are continuous at the surfaces and that as the distance from the surfaces increases, these fields approach zero. The magnetostatic solution also requires that the magnetostatic equation of motion, repeated below, be satisfied:

$$\dot{\vec{M}} = \gamma(\vec{M} \times \vec{H}) \quad (4)$$

Damon and Eshbach's solutions for the slab geometry yield important insights into the magnetostatic modes. First of all, they found that two frequency dependent magnetostatic modal solutions exist. In the preceding spin system description, the mode is characterized by energy densities that exist throughout the volume. This is the so-called volume or "bulk effect" mode where the

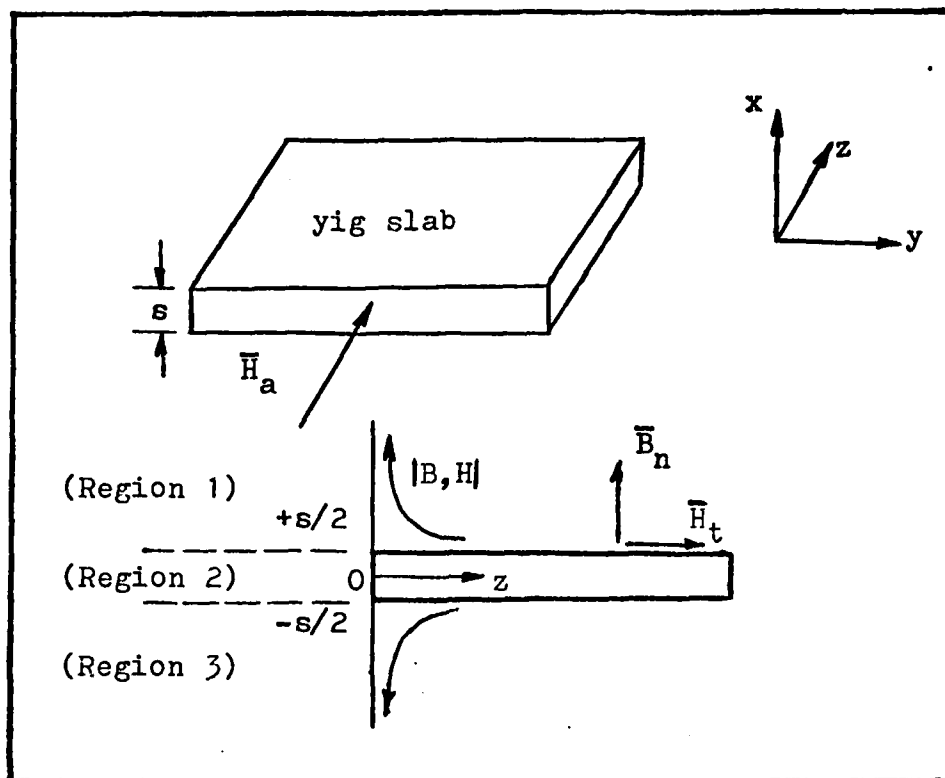


Figure 2. Damon and Eshbach Theoretical Slab and Boundary Conditions.

energy propagation mechanism is due to spin exchange coupling. One of the Damon and Eshbach solutions fits this particular mode. However, another solution which is of particular interest is characterized as a surface mode where the energy densities are at their greatest at the slab surfaces. Although the exact mechanism for this "surface guided mode" (Ref 10:17) is difficult to

explain, it is characterized by being primarily non-reciprocal and with positive dispersion. As presented by Damon and Eshbach, this modal solution can be expressed in terms of the following relation (Ref 4:313):

$$\Omega_o^2 = \Omega_H^2 + \Omega_H + [2 + 2 \coth (ks)] \quad (7)$$

where $\Omega_o = \omega / 4\pi M_s \gamma$

$\Omega_H = H_e / 4\pi M_s$

$k =$ the MSSW wave vector number

$s =$ the slab thickness

$\omega =$ the MSSW angular frequency

$\gamma = 2\pi(2.8 \times 10^6)$ rad/Oe-sec

Making the indicated substitutions yields the expression used by Brundle and Freedman (Ref 2:133):

$$\left(\frac{\omega}{\gamma}\right)^2 = H_e^2 + 4\pi M_s H_e + \frac{1}{4}(4\pi M_s)^2 (1 - e^{-2ks}) \quad (8)$$

An analysis of Eqn (8) shows that the ω versus k relation as plotted in Figure 3 is positive, increasing monotonically. This dispersion relation describes the magnetostatic surface wave (MSSW) mode.

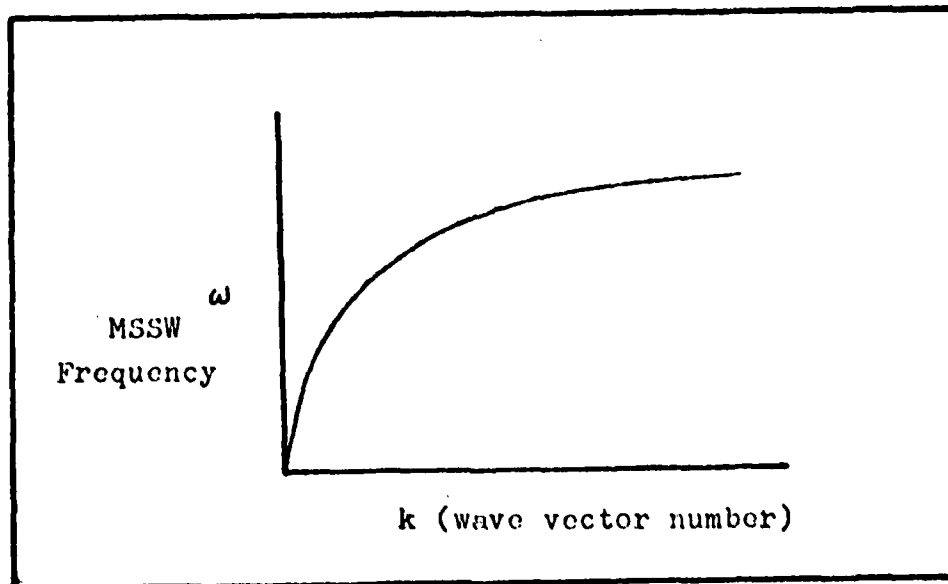


Figure 3. General Dispersion Curve for MSSWs

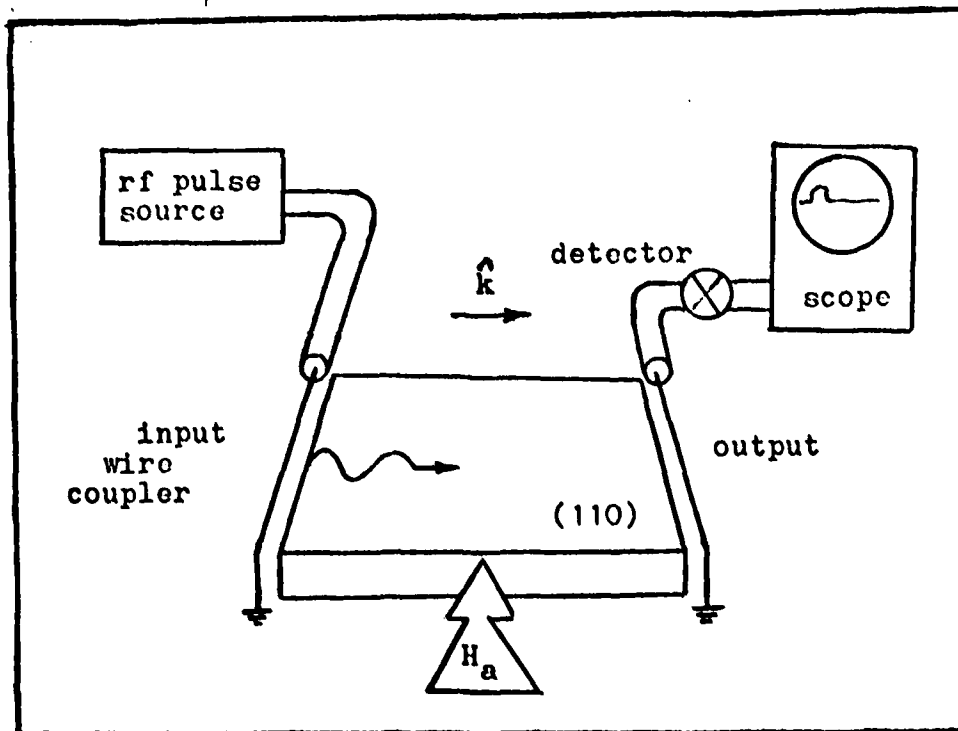


Figure 4. Brundle and Freedman Experiment.

Experimental Observation of MSSWs on a Slab

In 1968, Brundle and Freedman experimentally excited and observed MSSW propagation on a YIG slab 4.2 mm wide, 8.5 mm long, and 0.5 mm thick. Two tests were devised to observe MSSW effects. One test was a pulse experiment where group delay was measured. The second test was a c.w. test where standing waves were produced by allowing the surface waves to travel completely around the slab. Analysis of the MSSW mode was based on the dispersion solution shown as Eqn (8). Figure 4 shows the experimental set-up used by Brundle and Freedman. Additionally, it was pointed out that the actual group velocity differed from the theoretical group velocity, $v_g = \partial\omega/\partial K$, due to the dispersion and lossiness of the particular slab used. However, proof of the existence of the surface wave on the slab was attained by observing the effect of a conductive plate held next to the slab surfaces.

According to Damon and Eshbach's results, surface waves would propagate, as depicted in Figure 5, in a direction, \hat{k} , determined by

$$\hat{k} = \frac{\bar{H}_e}{|\bar{H}_e|} \times \hat{n} \quad (9)$$

where \hat{n} is the surface normal unit vector. This implies that the non-reciprocal nature of the surface wave would result in propagation in only one direction relative to the applied field and surface of interest. In fact when the metal plate in Brundle and Freedman's experiment was placed next to one surface, no significant effect was seen on the surface wave. However, when the metal plate

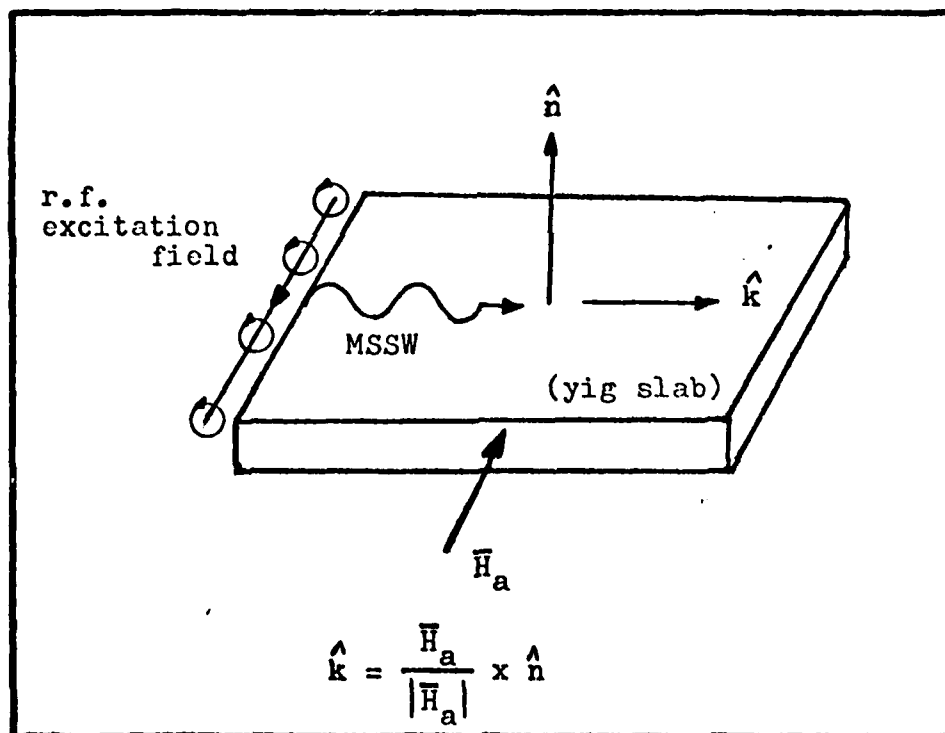


Figure 5. MSSW Propagation Direction, \hat{k} , Relative to \bar{H}_a and \bar{H}_{rf} .

was placed next to the opposite surface, the surface wave disappeared. These results and the implied surface wave propagation direction agreed with the predicted one as calculated by Eqn (9).

MSSWs on a YIG Ring

In 1974, Sethares investigated the potential excitation of magnetostatic surface waves on a thin film YIG ring (Ref 10). The ring film was produced using a liquid phase epitaxy process. Several rings were produced with varying thicknesses ranging from approximately four to ten microns. All rings were produced using a gadolinium-gallium-garnet (GGG) substrate.

It was Sethares' prediction that if the surface wavelengths were small compared to the ring geometry then the ring surface would approximate a slab geometry. Thus, the dispersion relation as used by Brundle and Freedman would be applicable. Figure 6 describes the experimental set up used by Sethares (Ref 10).

Sethares' results were significant in three ways. First, MSSW propagation supported by the thin film ring using simple, fine wire couplers was observed. Second, propagation was in a complete path around the ring circumference with wavelengths smaller than the ring dimensions. Finally, the relative amplitude of the surface wave pulse

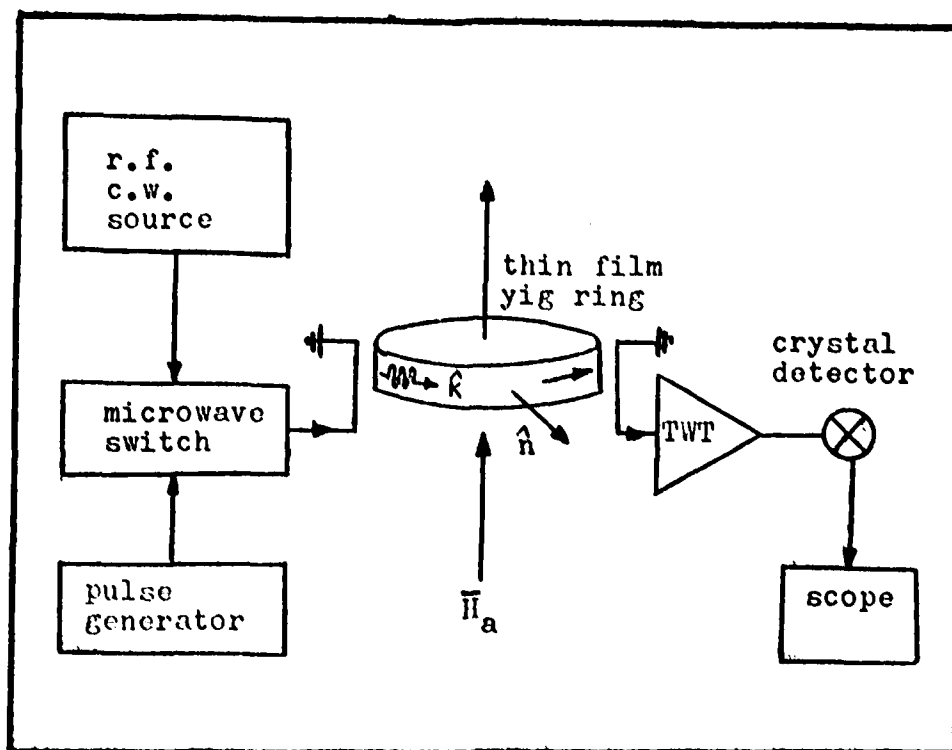


Figure 6. Basic Group Delay Experiment
Used by Sethares.

varied considerably with the angular position of the ring (Ref 10:40). Obviously, this result was not desirable, since it implied possible degradations in rotation rate sensing. With closer examination of the thin ring, Sethares observed a "facetting" of the thin film surface. This kind of variation in the vicinity of the coupling probes was speculated to be the source of the amplitude variations. Subsequently, Sethares recommended that a

high quality single crystal YIG boule be cut and polished into a suitable ring geometry in order to avoid the problem encountered with the thin film ring.

Sethares' also pointed out that other factors may affect the propagation characteristics. Loss can be attributed to both frequency independent and dependent factors as expressed as

$$\alpha = Af + B \quad (10)$$

where α represents the combined loss due to factors A and B. The frequency dependent factor, A, is attributed to intrinsic Kasuya-LeCraw mechanisms. Surface and volume deformities are associated with the frequency independent factor, B (Refs 11:13 and 14:147-157).

As can be seen from this discussion there are many factors affecting the MSSW propagation along with the ring versus slab assumption. In addition, there was no complete model that would represent the actual ring characteristics. This dilemma required special consideration in approaching the rotation rate sensor designs and their respective design parameters.

III. Magnetostatic Rotation Rate Sensing

General Concept

The chief motivation behind any improved rotation rate sensing system is to devise a scheme where the system output becomes related to the applied rotation rate in a linear and highly sensitive manner. The relationship then involves a scaling or sensitivity function which in its simplest form may be stated as

$$y(\Omega) = S(\rho_i) \Omega \quad (11)$$

In Eqn (11), $y(\Omega)$ is the system output. $S(\rho_i)$ is the scaling function which is a function of the fixed system parameters, ρ_i , and the applied rotation rate, Ω .

Since an important design objective is to maximize the scale factor, any new technology which promises such improvement is worth investigating. For instance, consider the 1974 AFCRL proposal for using magnetostatic surface waves to sense rotation rates. This proposal asserted that due to the slow MSSW propagation velocities, very sensitive scale factors on the order of 10^{-4} rad/rad/sec could be achieved (Ref 8). Here the system output is related to the input rotation rate as a net phase shift of the MSSW.

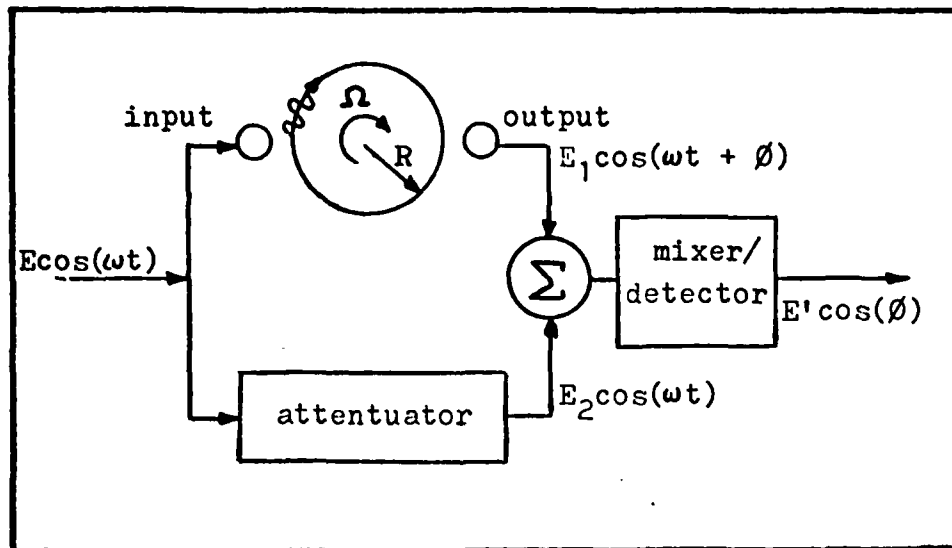


Figure 7. Simplified Phase Sensor.

Phase Sensitive Sensor Equations

An analysis of an MSSW phase sensitive rotation rate sensing system can be developed by analyzing the simple system shown in Figure 7. With the ring stationary relative to the body-fixed coordinate frame, the surface wave launched from the input probe will travel to the output probe in time, t_r , where

$$t_r = \pi R / v_p \quad (12)$$

where v_p = the MSSW phase velocity

R = the ring radius

If the ring is allowed to rotate at some angular rate, Ω , the time of propagation, t_2 , is now influenced by the tangential velocity component, $\vec{v}_t = \vec{\Omega} \times \vec{R}$, so that the net velocity becomes the vector sum

$$\vec{v} = \vec{v}_p + \vec{v}_t \quad (13)$$

Using this relation, the time difference, Δt , can be written as

$$\Delta t = t_1 - t_2 = \frac{\pi R^2 \Omega}{v_p^2 (1 + R\Omega/v_p)} \quad (14)$$

Since, the change in phase for the surface wave can be related to the application of Ω and the propagation time via the wave frequency, f , Eqn (14) becomes

$$\Delta \phi = 2\pi f \Delta t \quad (15)$$

This yields an expression for the net phase shift, neglecting any phase bias, so that

$$\Delta \phi = \frac{2\pi f (\pi R^2 \Omega)}{v_p^2 (1 + R\Omega/v_p)} \quad (16)$$

If in Eqn (16) the higher order effect term in the denominator is neglected under the assumption that the tangential velocity is small compared to the MSSW phase velocity (this may not always be the case), the scale factor extracted from Eqn (16) becomes a function of the ring radius, MSSW frequency, and phase velocity. This is expressed as

$$\Delta\phi = S_{\phi}(R, f, \Omega) \quad (17)$$

where

$$S_{\phi} = \frac{\pi R^2 (2\pi f)}{v_p^2} \quad (18)$$

With the ring radius and MSSW frequency held constant the scale factor then varies inversely with the square of the phase velocity. Since MSSW propagation can be varied to produce slow phase velocities, the rationale behind the AFCRL proposal becomes obvious. However, since the propagation is relative to the input and output probes, the rotation rate measurement is strictly relative and noninertial.

Frequency Sensitive Sensor Equations

In the sense of an alternate scheme to sense rotation rates using surface waves, a system can be devised where the rotating ring is part of an oscillator system. In this

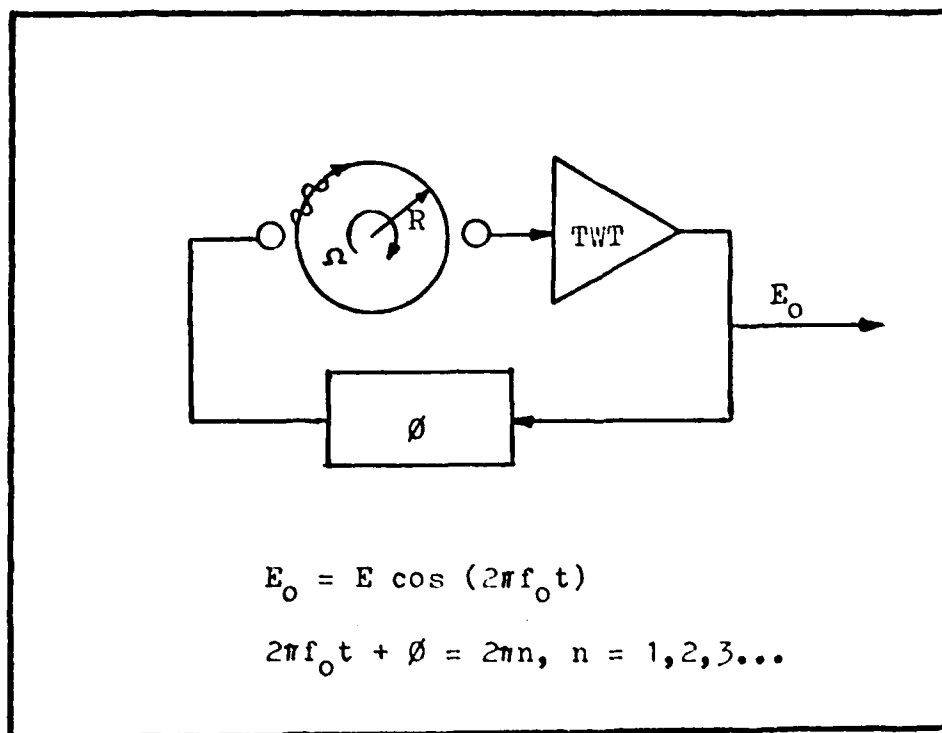


Figure 8. Simplified Frequency Sensitive Sensor.

scheme, a change in oscillator frequency, Δf , becomes a measure of the applied rotation rate where the scale factor can still be expressed as a function of the ring radius, MSSW frequency, and phase velocity:

$$S_f = f(R, \Omega, f) \quad (19)$$

An exact expression for the scale factor can be derived by inspecting the simple oscillator system shown in Figure 8. Based upon a MSSW arriving in phase at some reference point, the system will oscillate when the following condition is met (Ref 7):

$$2\pi ft + \phi_e = 2\pi n, \quad n=1,2,3,\dots$$

Or

$$ft = n - \frac{\phi_e}{2\pi} \quad (20)$$

where f = the oscillator frequency

ϕ_e = the phase error or bias in the loop

t = phase propagation time

In Eqn (20), the time, t , is a function of the total surface wave velocity and the path length assuming that the phase velocities of the remaining oscillator components are fast compared to the ring. For the case when the ring is stationary, $t = L/v_p$, where L is the ring propagation path length. Substituting this into Eqn (20) yields

$$f = \frac{v_p}{L} \left(n - \frac{\phi_e}{2\pi} \right), \quad n=0 \quad (21)$$

For the dynamic case where the ring is allowed to rotate, the phase velocity is modified by the tangential

velocity component as was the case for the phase sensitive sensor system. The application of the rotation rate then causes a shift in the oscillator frequency so that

$$f + \Delta f = \frac{v_p + R\Omega}{L} \left(n - \frac{\phi_c}{2\pi} \right) \quad (22)$$

where $f + \Delta f$ assumes a net increase in the wave velocity and corresponding decrease in the propagation time. This accounts for a Δf where by substituting Eqn (21) into Eqn (22) yields

$$f + \Delta f = f + \frac{R\Omega}{L} \left(n - \frac{\phi_c}{2\pi} \right) \quad (23)$$

Or

$$\Delta f = \frac{R\Omega}{L} \left(n - \frac{\phi_c}{2\pi} \right) \quad (24)$$

Eqn (24) can be further simplified using Eqn 21 again:

$$\Delta f = \left(\frac{Rf}{v_p} \right) \Omega \quad (25)$$

Again, as was done for the phase sensitive sensor, the scale factor can be extracted:

$$S_f = \frac{Rf}{V_p} \quad (26)$$

It is interesting to compare the two scale factors of Eqns (18) and (26). By forming the ratio of S_f/S_ϕ , the frequency sensitive sensor can be seen to be more sensitive than the phase sensor:

$$S_f = \frac{V_p}{2\pi^2} S_\phi \quad (27)$$

Both functions, however, remain dependent on the MSSW phase velocity. But, this velocity is frequency dependent due to the dispersive nature of MSSW propagation; therefore, additional analysis is still required to relate the actual MSSW behavior to the rotating ring. One way of doing this is to measure MSSW group effects to ascertain the actual ring's dispersive properties.

MSSW Relations

In the preceding sections of this chapter, the rotation rate sensor scale factors were derived as functions of ring geometry, MSSW frequency, and phase velocity. These functions imply a frequency dependence of the phase velocity

which implies the dispersion relation of the MSSW modes. This relation as previously stated is

$$\left(\frac{\omega}{\gamma}\right)^2 = H_e^2 + 4\pi M_s H_e + \frac{1}{4}(4\pi M_s)^2(1 - e^{-2ks}) \quad (8)$$

With the phase velocity defined as $v_p = \omega/k$, Eqn (8) can be manipulated to yield

$$v_p = 2\omega s \left\{ \ln \left[\frac{1/4(4\pi M_s)^2}{(H_e + 2\pi M_s)^2 - (\omega/\gamma)^2} \right] \right\}^{-1} \quad (28)$$

However, before Eqn (28) can be applied to the scale factor equations, values for the effective field, H_e , and the surface wave frequency, ω , must be determined. Although this could be done analytically, it is more practical, considering unknown anisotropic effects, to empirically measure the actual MSSW ring parameters. Under the assumption that the ring is high in quality and not excessively lossy, the determination of the MSSW parameters can be conveniently accomplished using group delay measurements.

Consider, for example, the system described in Figure 6 used to measure group delay. Other than the fact that the YIG geometry is a ring, the set-up is basically the

same as used in the Brundic and Freedman experiment. The object is to have the ring biased by a fixed, known DC magnetic field and to launch a MSSW pulse from the input probe onto the ring. The propagation direction is parallel to the cross-product of $\vec{H} \times \hat{n}$. The microwave source frequency is adjusted until an acceptable, delayed pulse is received at the output probe. Input power is limited to avoid nonlinear behavior (Ref 3:427-428). After determining the intrinsic delays due to equipment and line group velocities, the actual MSSW group delay is found. Since the MSSW group velocity can be found by dividing the traveled path length by the MSSW group time delay, this can be compared to the theoretical group velocity where $v_g = \frac{\partial \omega}{\partial k}$. Eqn (8) can then be used to show that

$$v_g = \frac{r^2 s}{\omega} \left[(H_e + 2\pi M_s)^2 - (\omega/r)^2 \right] \quad (29)$$

where s = the YIG ring thickness

ω = the microwave source angular frequency

Solving Eqn (29) for the effective field yields:

$$H_e = \left[\left(\frac{\omega}{r} \right)^2 + \frac{v_g \omega}{r^2 s} \right]^{1/2} - \frac{1}{2}(4\pi M_s) \quad (30)$$

Additionally, a more explicit relation relating the desired phase velocity to the actual group velocity can be found by substituting Eqn (29) into Eqn (28). This yields the expression:

$$v_p = 2\omega S \left\{ \ln \left[\frac{1/4 (4\pi M_S r)^2 S}{\omega v_g} \right] \right\}^{-1} \quad (31)$$

Since Eqn (31) shows the dependence of the phase velocity on the MSSW frequency, another piece of useful information would be the allowable frequency range over which surface waves exist for a given DC biasing field. That range of frequencies includes all surface wave vector numbers for $0 \leq k \leq \infty$. Applying these limits to the dispersion relation, Eqn (8), yields an upper and lower bound where

$$f_{LO} = \frac{\gamma}{2\pi} \left[H(H + 4\pi M_S) \right]^{1/2} \quad (32)$$

and

$$f_{HI} = \frac{\gamma}{2\pi} \left[H + 1/2 (4\pi M_S) \right] \quad (33)$$

Thus, knowledge of the group delay of the MSSW pulse and how it varies with frequency provides insights into the dispersive character, effective field strength, and MSSW frequency range of the ring for a given DC field. With this knowledge, the scaling functions for the phase and frequency sensitive rotation rate sensing systems can be can be evaluated.

IV. MSSW Rotation Rate Sensor Design

General Design Aspects

As indicated in the preceding sections, the experimental work in support of this thesis is centered around two different rate sensing schemes. In one scheme, the phase shift, $\Delta\phi$, is the desired system output determined by the MSSW ring geometry and its parameters as well as ring rotation rate. This system is a basic interferometer where the phasing of the MSSW signal is allowed to interfere with the input reference signal. This produces a voltage which is proportional to the applied rotation rate via some scaling function. In another scheme, a microwave oscillator is built around the phase delay characteristics of the ring. The frequency shift, Δf , of the oscillator is a measure of the applied rotation rate which, again, is affected by a scaling function.

For both rate sensing schemes, a thick, high purity single crystal ring is used. The ring specifications are listed in Table I. Note that such parameters as linewidth, anisotropic field and demagnetization field effects were not known; however, the following assumptions were made:

- (1) The MSSW ring loss was low.
- (2) The ring linewidth was well less than 1 Oc.

TABLE I

Thick YIG Ring Specifications

Construction	High purity, single crystal yttrium-iron-garnet (yig) sleeve on a plexiglass dielectric bushing.
Dimensions	Yig ring: O.D. = 1.270 cm thickness = 0.128 cm width = 0.381 cm
	Bushing: O.D. = 1.014 cm I.D. = 0.635 cm width = 0.381 cm
Linewidth	H assumed less than 0.5 Oe.
Demagnetization Factor	N_d assumed: $0.3 \leq N_d \leq 0.5$
Loss	Assumed low
Anisotropic Effects	Assumed negligible
Saturation Magnetization	$4\pi M_s = 1750$ Oersteds

(3) Anisotropic field effects are negligible compared to the applied and demagnetizing fields.

(4) The demagnetization factor for the ring is between 0.3 and 0.5 and can be determined empirically.

Another design aspect is the magnetic biasing field, H_a . Since the YIG is in a ring geometry, and the desired propagation path is around the ring's periphery, H_a must be applied parallel to the ring's axis of revolution. This requires a mounting scheme that provides for this field orientation. The scheme must also provide for RF excitation parallel to the ring periphery. Figure 9 shows the physical configuration that satisfies these requirements with MSSW propagation satisfying Eqn (9).

Finally, these experiments required a pair of RF magnetic transducers or probes capable of inducing and detecting the MSSW signal on the ring. The design criteria chosen for the probes are that the input probe must be capable of producing a highly localized excitation that is primarily magnetic in nature and the output probe must be able to satisfactorily detect the MSSW magnetic field at some point along the MSSW path. Another important aspect is that the RF isolation between the probes be high so as to prevent unwanted corruption of the MSSW output signal.

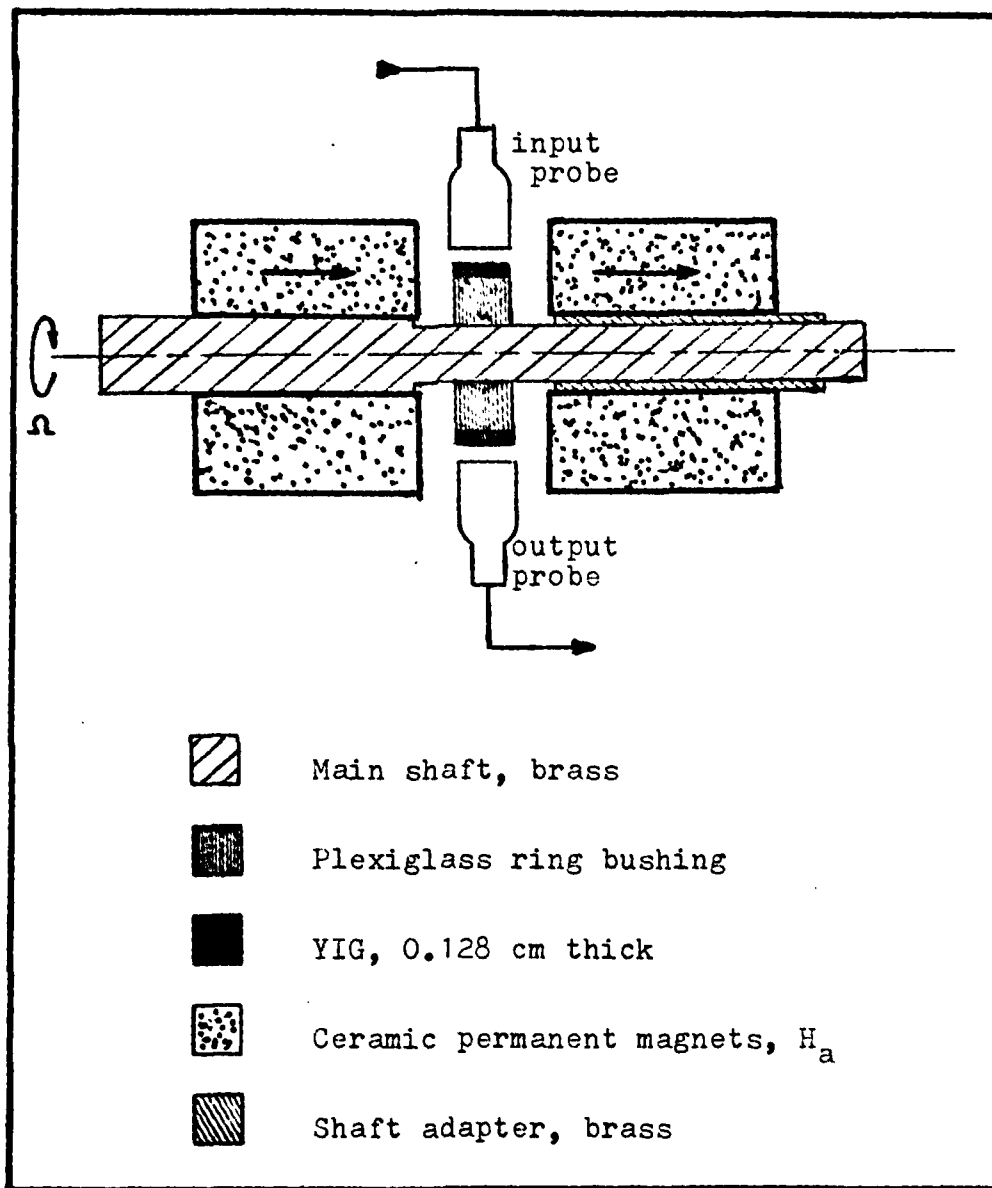


Figure 9. Cross-sectional View of MSSW Ring Configuration.

Probe Design

Previous experiments and analysis performed by Sethares and others (Refs 1, 2, 3, 7, 11) were done with various RF excitation methods. The simplest, as used by Brundle and Freedman in their work, consists of a pair of fine wires extended across the YIG surface and terminated to ground. RF double stub tuners are often employed in these schemes to ensure line matching and high coupling efficiency. Another often employed method involves coupling to the YIG material via micro-strip designed for impedance matching. Both of the aforementioned schemes are acceptable; however, in order to couple to the rotating YIG ring, wire-type couplers configured in a shielded probe construction were chosen. Such a probe design was desired, since it offered the ability to easily adjust coupling distance to the ring as well as providing potentially high isolation. These advantages are gained, however, at the possible sacrifice of coupling efficiency.

Since a purely analytical design of the RF probes would require an evaluation of the complex fields in the vicinity of a magnetically radiating RF field element near an anisotropic, ferromagnetic medium, the probe design task was approached heuristically.

To elicit maximum radiation as well as detection sensitivity, the coupler was viewed in the sense of the Biot-Savart Law where:

$$\vec{H} = \oint \frac{I d\vec{L} \times \hat{a}_R}{4\pi R^2} \quad (34)$$

The practical implication of this law is that the current loop of the probe should provide a maximum enclosed area. Unfortunately, maximum enclosed loop area also implies maximum radiation and detection of stray energies. This is further complicated by the dimensions of the loop in terms of signal wavelengths. This problem can be somewhat alleviated by applying RF shielding to the loop at those places where radiation and detection are not desired. In practice this involves the provision of a low resistivity, conducting boundary tied to ground potential to "sink" unwanted tangential \vec{H} fields. In summary, these two basic ideas, maximum loop area and tangential \vec{H} field shielding, were used to design the RF probes used in both the phase and frequency sensitive experiments.

Another aspect of probe design is the practical range of surface wave vector numbers that can be induced. Although low order wave vector (k) numbers are relatively easy to generate, it is the higher order numbers which

correspond to the high energy densities and slow propagation velocities that are desired. These k-numbers are a function of the probe wire diameter, d_p , and can be expressed as

$$K = \frac{2\pi}{\lambda_p} , \quad 2d_p < \lambda_p < \infty \quad (35)$$

where λ_p values are the wavelengths that the wire is capable of practically producing (Ref 11:35) based on d_p . In practice, it has been found that due to loss effects, the wire diameter should be corrected by a factor of approximately 0.8.

Selection of a probe wire diameter must also consider the range of k-numbers that the ring itself is capable of supporting. This is a function of the YIG thickness, s , where, according to Sethares, the useful range is

$$0 \leq Ks \leq 1 \quad (36)$$

Using a YIG thickness of 0.128 cm yields a maximum k-number of approximately 7.8 cm^{-1} . Considering this approximate limit, a probe wire diameter of 0.01 in. was selected where according to Eqn (35) wave numbers as high

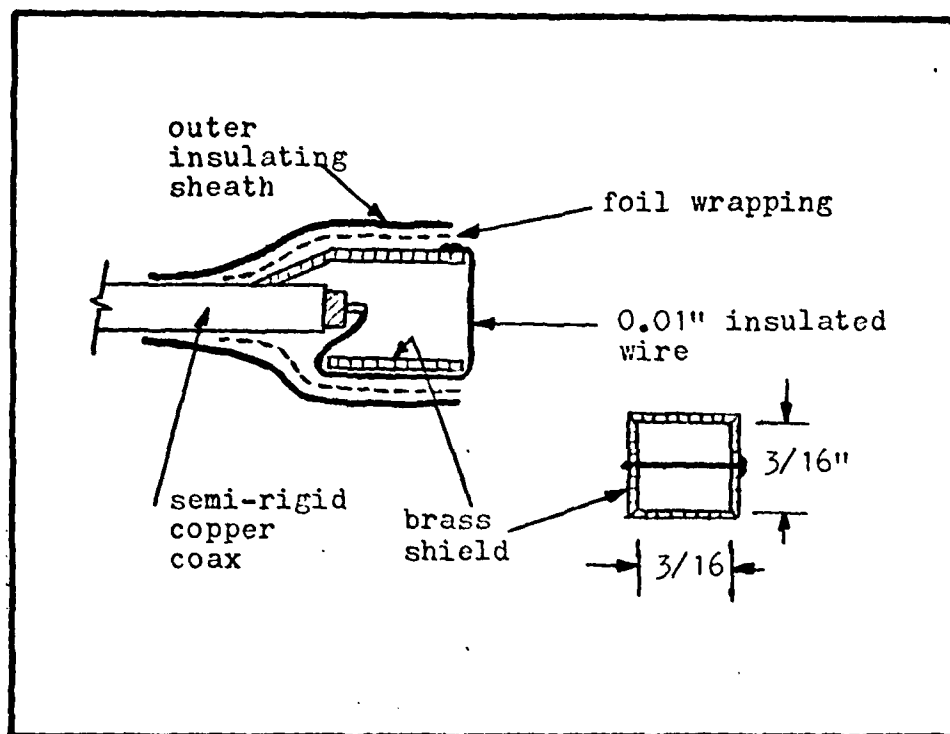


Figure 10. Cross-sectional View of RF Probe.

as 154 cm^{-1} could be produced. Therefore, the probe would not be the limiting factor in high wave number generation.

The result of this approach is the probe configuration shown in Figure 10. Evaluation of this design is included in the Results section of this thesis.

Rate Sensor Design Factors

Figures 11 and 12 show in block diagram form the experimental set-ups used for the $\Delta\theta$ and Δf MSSW rotation

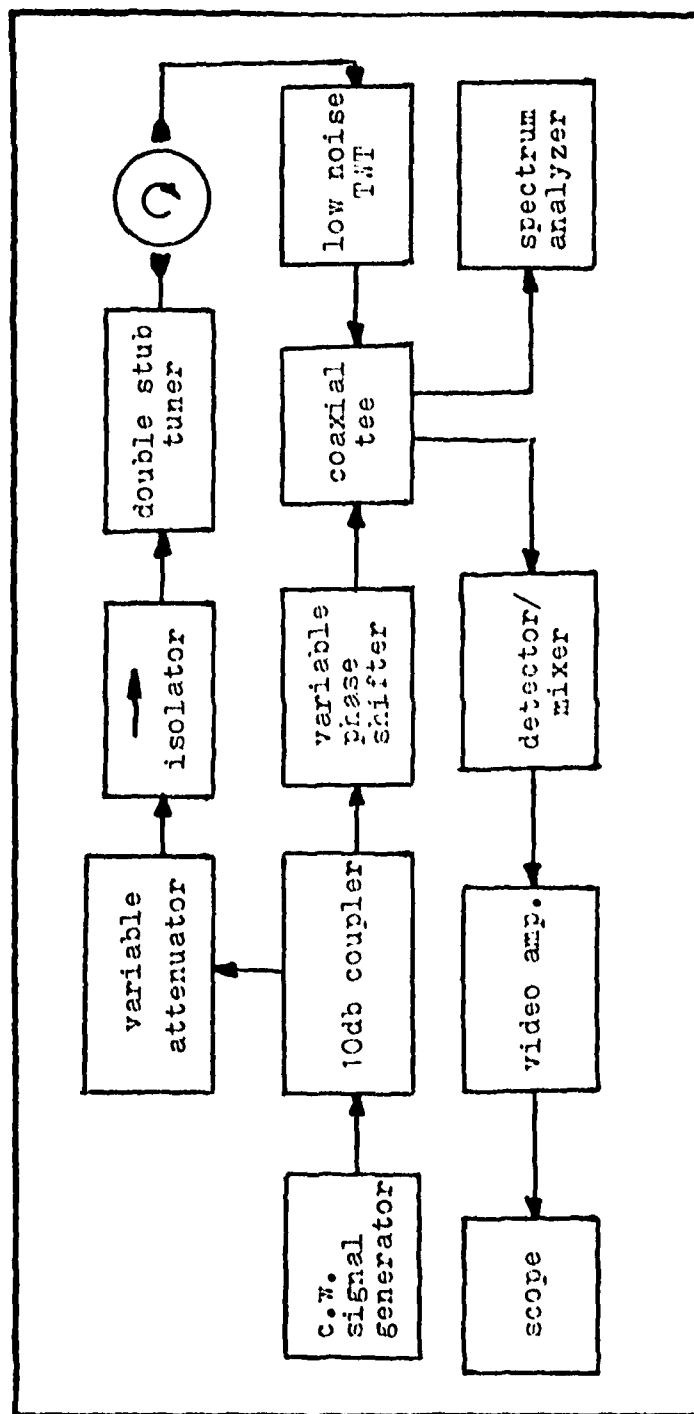


Figure 11. Block Diagram of Phase Sensitive Sensor.

rate sensing. In the $\Delta\phi$ scheme, a single signal generator provides both a reference signal and excitation for the MSSW input probe. The double stub tuner is used to maximize the coupling efficiency of the probe. The output signal off the ring is amplified by a wideband, low noise traveling wave tube (TWT) amplifier from which it is summed together with the adjusted reference signal. When the ring is stationary, the reference signal's amplitude and phase are adjusted for a minimum detector signal. Due to the nonlinear detector characteristic and inherent low pass filtering, an interference signal whose amplitude is proportional to the phase difference between the adjusted reference signal and the MSSW output signal is produced where

$$E_o = E_o' \cos(\Delta\phi) \quad (37)$$

and

$$\Delta\phi = \frac{2\pi f \Omega (\pi R^2)}{v_p^2 (1 + R\Omega/v_p)} \quad (36)$$

This set-up also provides a second output port where the spectral purity of the MSSW and reference signals can be observed.

In the Δf scheme shown in Figure 12, a MSSW ring oscillator consisting of gain and phase adjustments, a

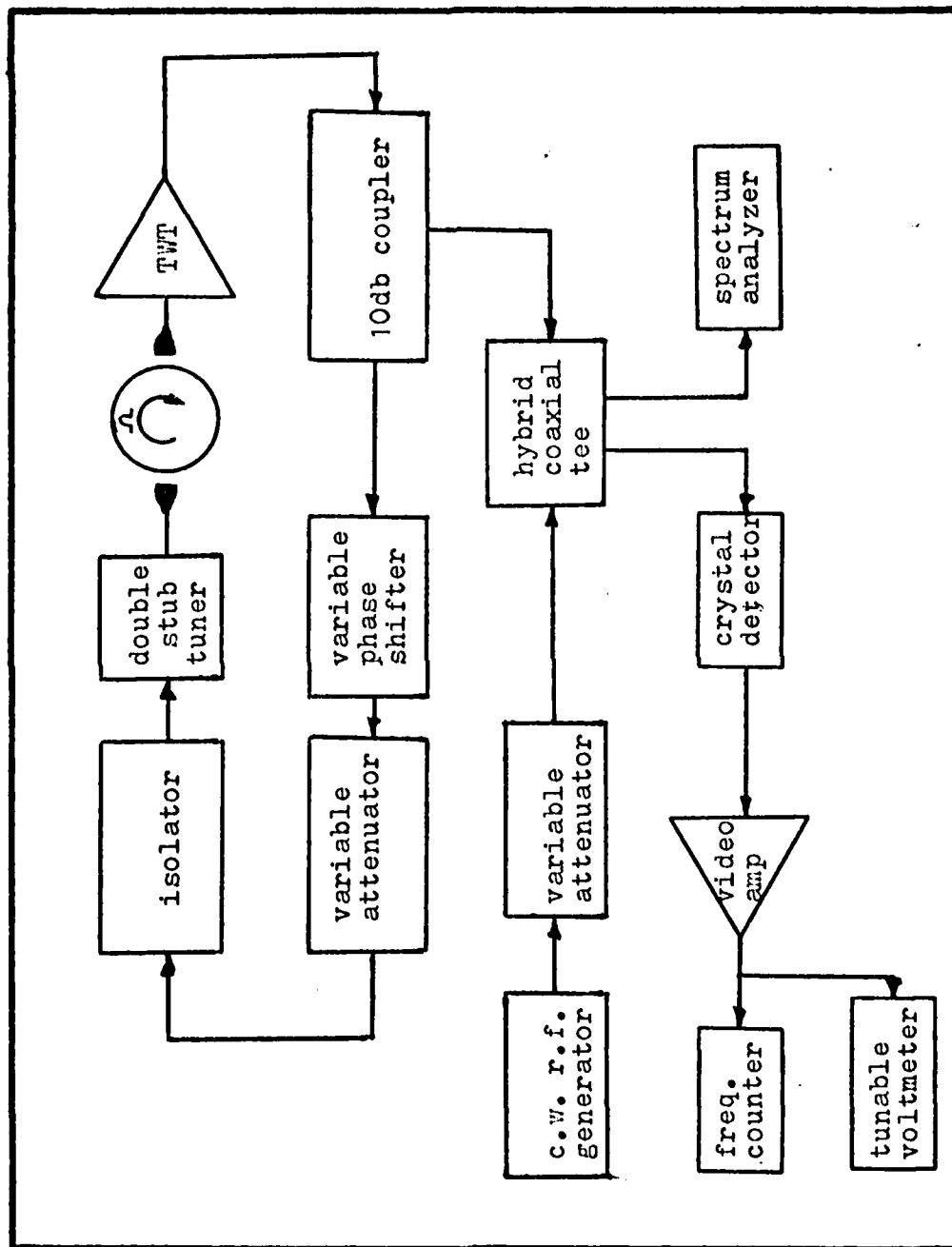


Figure 12. Af MSSW Rate Sensor

double stub tuner for maximizing input coupling efficiency, and an output coupler generates a RF signal which is compared to a reference signal, f_r . When the ring is stationary, the signal generator is adjusted to equal the amplitude and phase of the output oscillation frequency of the ring oscillator. The non-linear detector is used as a mixer where its output is filtered and further amplified. For shifts in the oscillator frequency due to an applied rotation rate, the detected Δf is measured using a frequency counter. A tunable voltmeter is also provided to further filter the signal and measure relative strength. Again a second output port is available from the coaxial tee so that the spectral purity and frequency shift of the system output can be monitored.

For each of these two rate sensing schemes, it is important to determine the following magnetostatic and rate sensing parameters:

- (1) The MSSW dispersion relation.
- (2) The actual effective field, H_e .
- (3) The probe isolation, I_p .
- (4) The system insertion losses, L_i .
- (5) The theoretical scaling functions, S_ϕ and S_f .

In order to identify these parameters, the set-up in Figure 13 was used to measure the group delay of the

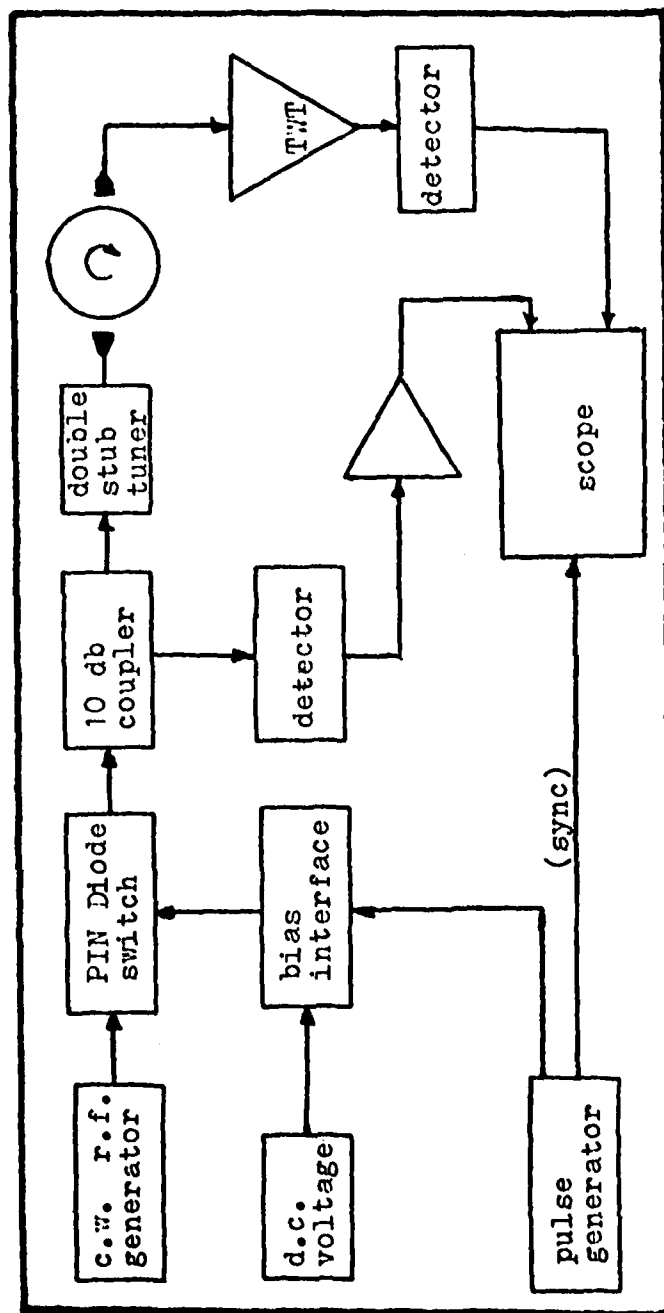
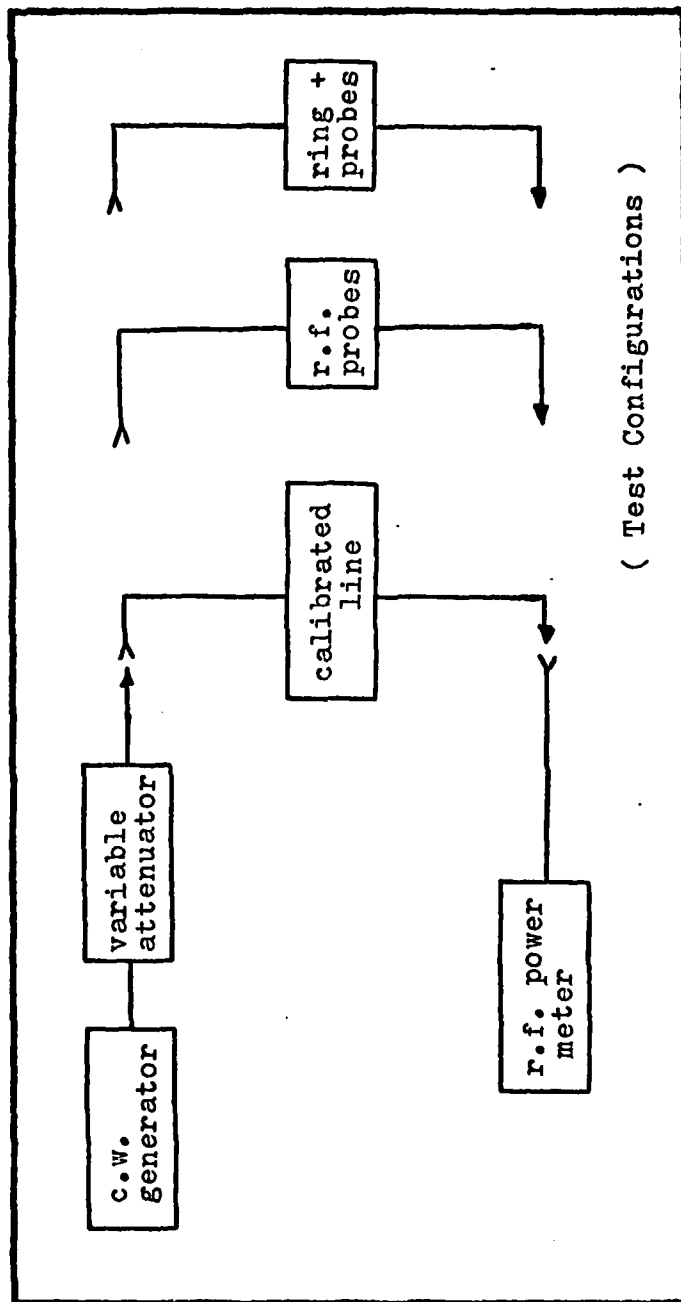


Figure 13. Group Delay Set-Up.

system as a function of frequency. Initially, the ring specifications listed in Table I and Eqn (8) were used to calculate the theoretical dispersion relationship. Here, an effective field of 300 Oe which provides a MSSW frequency range between 2.0 and 4.0 GHz was chosen. This data is listed in Table II. The theoretical limits for the frequency range of MSSW activity is seen to range from 2.2 to 3.3 GHz. The next step is to take this data and experimentally profile the probe isolation and system insertion losses using the set-up in Figure 14 and, then, measure the MSSW group delay as a function of frequency. The group velocity is calculated from

$$V_g = L/t_{\text{delay}} \quad (38)$$

where L is the propagation path length taken to be one half of the ring circumference. As previously explained in Section III, this information can be used to find the effective field, H_e , and the phase velocity of the system as a function of frequency. The scale factors, S_ϕ and S_f , can then be calculated and compared to theoretical values. Referring to Table II and using a k-number of 30 cm^{-1} , an applied rotation rate of 3000 RPM with a phase velocity of about $7.0 \times 10^8 \text{ cm/sec}$ at 3.29 GHz yields a phase shift of



(Test Configurations)

Figure 14. Loss Measurement Set-Up

TABLE II

Theoretical Dispersion Values for Thick Ring

frequency (G Hz)	k-number (cm^{-1})	group velocity ($\text{cm}/\mu\text{sec}$)	phase velocity ($\text{cm}/\mu\text{sec}$)
2.196	0	2200	∞
2.688	2	1080	8450
2.944	4	589	4620
3.087	6	337	3230
3.170	8	196	2490
3.219	10	116	2020
3.247	12	68.9	1700
3.265	14	51.1	1470
3.275	16	24.5	1290
3.281	18	14.7	1150
3.285	20	8.78	1030
3.287	22	5.26	939
3.288	24	3.15	861
3.289	26	1.89	795
3.290	30	0.687	689
3.290+	34	0.243	608
$H_0 = 300$ Oersteds		$s = 0.128$ cm.	

(2.67 x 10⁻⁶ radians and a frequency shift of nearly 1000 Hz. Actual measurement of these values requires a very low noise environment. Note that all of the above calculations are based on the application of the dispersion relation as developed for a slab geometry, therefore, this approximation for parameter identification for the ring geometry will match theory only with the generation of high k-numbers where the MSSW wavelenghts become small as compared to the YIG ring dimensions. Under this condition there should be no significant difference between a flat and ring geometry.

V. Experimental Results

General

During the experimentation phase of this thesis, the physical configuration of the thick YIG ring, the applied biasing field, and mounting hardware were carefully maintained. In all cases, the biasing field was allowed to rotate with the ring with a measured field strength of 750 Oersteds. Assuming a ring demagnetization factor of 0.3, the net effective field, H_e , was calculated to be on the order of 225 Oersteds. Using Eqns (32) and (33), the MSSW frequency range should extend from 2.0 to 3.15 GHz. Over this frequency range, it was hoped that group delays on the order of microseconds would be detected assuming ideal "loss conditions." These slow velocities would occur at the upper end of the frequency range where the MSSW wavelengths would be small compared to the ring dimensions; therefore, the slab dispersion relations used by Damon and Eshbach and Brundle and Freedman would hold true.

To allow for inevitable parameter uncertainty (e.g. demagnetization factor and slab versus ring geometry model disparities), experimental data was used to empirically determine the actual MSSW ring performance

TABLE III

MSSW Experimental Set-Up Parameters and Ranges

MSSW Fields	Applied, H_a , = 750 Oe. Demagnetization = 0.3 (assumed) Net effective field, H_e , = 225 Oe
Expected MSSW Frequencies	2.0 to 3.15 GHz based on H_e and MSSW ring saturation magnetization
Input Signal	Pulse or c.w. from 2.0 to 4.0 GHz Maximum power +3.0 dbm (calibrated) Pulse capability of 50 to 100 nsec at 50 KHz repetition rates
Output Signal	R.F. amplification of 36 db over 2.0 to 4.0 GHz range plus additional 40 db voltage gain of detected video.
Applied Rotation Rates	0 to 3000 RPM (cw or ccw)

parameters. This experimental modeling was done via group delay measurements with nominal 100 nanosecond wide microwave pulses with peak powers of no more than +3.0 dbm and at a 50kHz repetition rate. When these pulses were applied

to the MSSW ring via the RF probes, the detected output signal was amplified by a low noise, broadband traveling wave tube (TWT) which provided a nominal gain of 36 db over a 2.0 to 4.0 GHz frequency range. Additional voltage gain on the order of 40 db was available for further amplification of the detected video pulse. Table III summarizes the equipment capabilities and the initial MSSW operating parameters. Appendix II lists specific equipment used.

With these capabilities, the following objectives were pursued:

- (1) Determine the system losses including an evaluation of the RF probes designed and built for the experiments.
- (2) Identify the actual thick ring MSSW parameters using group delay measurement data.
- (3) Determine and evaluate the thick ring suitability as a MSSW rotation rate medium for both phase ($\Delta\phi$) and frequency (Δf) sensitive schemes. Also, identify any observed nonuniform behavior, its magnitude and probable source.

System Losses

Of initial interest was the probe isolation, I_p , over the expected MSSW frequency range; therefore, a preliminary inspection of the microwave frequency band from 2.0 to 4.0 GHz was made. The upper limit of the MSSW activity was seen to occur at about 3.2 GHz which was slightly higher than the estimated 3.15 GHz limit. Since the higher order wave vector (k) numbers were of interest, the frequency range was limited to 2.4 to 3.2 GHz. (Later, this range was further revised to 2.8 to 3.2 GHz based upon measured MSSW group delays.)

Isolation loss data on the probes was gathered using the general set-up shown in Figure 14, where the calibrated line measurements were made to compensate for line, connector, and equipment losses. Once data on the probes was collected, the YIG ring was inserted into the set-up and insertion loss data, which included probe coupling and ring propagation effects, was obtained. For both cases, the physical configuration was carefully maintained so that the only difference between the isolation and insertion set-ups was the presence or absence of the YIG ring.

As can be seen from the isolation loss data in Table IV, the probe-to-probe isolation I_p , remained well below 40 db. Separation between the probes was about 0.52" to

allow space for the YIG ring and the 0.01" probe coupling wires. Although probe VSWR was seen to be high (in some cases greater than 5.0), this was not considered detrimental since tuning stubs were to be used to compensate for impedance mismatches. Overall, the probes more than adequately demonstrated their ability to provide high isolation. Similarly, separate tests showed that the magnetic fields at the probe aperture were highly localized. For example, probes that were allowed to touch with the loop elements at right angles showed near field isolations in excess of 35 db. Consequently, the probes seemed suitable for the remaining experiments.

With the probe isolation loss calibrated, the ring was inserted into the experimental set-up to measure insertion losses. At 3.2 GHz, it was noted that the insertion loss varied considerably as the ring was rotated between the RF probes. This change was suspected to be a result of non-uniform MSSW behavior, and later it was seen that these variations correlated with MSSW pulse group delay data. This corruptive effect, which was a function of the ring angular orientation, was tracked throughout all experiments by labeling the point of minimum insertion loss as θ_1 and the point of maximum loss as θ_2 . The angular separation between these points

TABLE IV

MSSW System Losses

f (GHz)	ω (10^{10} rad/sec)	Isolation (db)	Insertion*	
			θ_1	θ_2
2.80	1.759	50.8	8.8	10.0
2.90	1.822	48.1	4.7	5.3
3.00	1.885	50.8	4.7	4.9
3.10	1.948	45.6	6.8	9.2
3.12	1.960	45.6	9.0	11.1
3.14	1.973	45.5	11.4	14.3
3.16	1.986	44.9	13.8	19.5
3.18	1.998	46.0	16.7	29.2
3.20	2.011	50.9	22.5	49.5
3.20+	2.011+	47.0	-	∞

Notes: * θ_1 position of minimum loss
and minimum time delay.
 θ_2 position of maximum loss
and maximum time delay.

+ Losses at over 3.2 GHz very
high, unmeasurable.

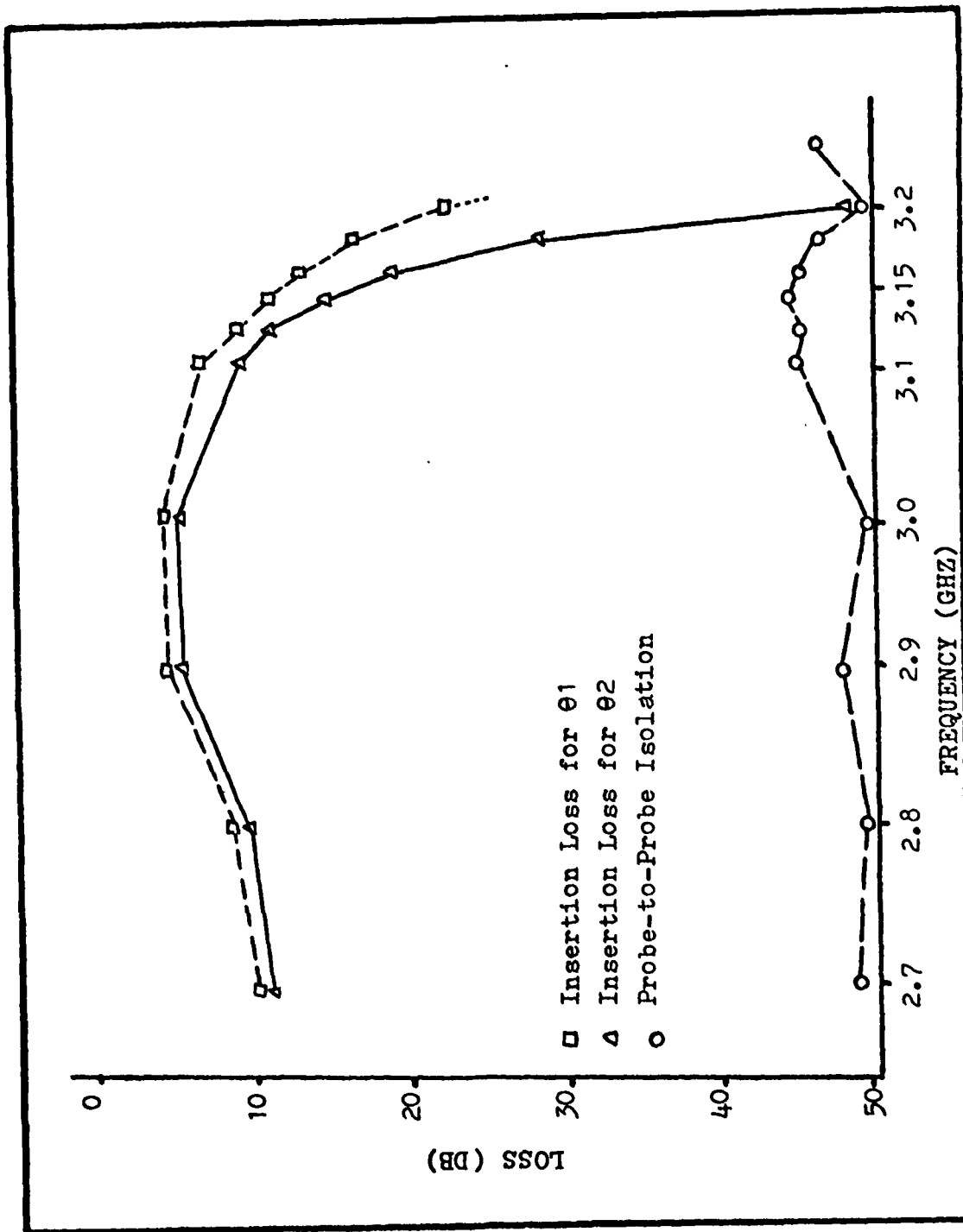


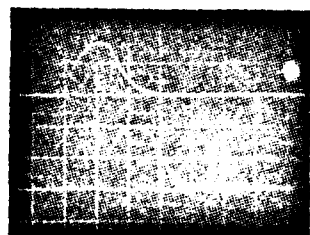
Figure 15. System Losses vs Frequency

was slightly less than 90° . No other locations were found that provided the same loss values; although variations in the insertion loss occurred over the entire 360° rotation of the ring. Loss data for the θ_1 and θ_2 positions is listed in Table IV and plotted in Figure 15.

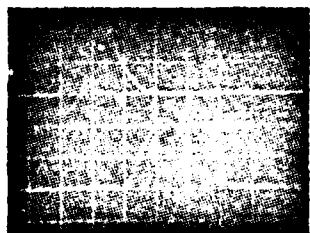
With knowledge of the probe performance and the ring losses, very high coupling efficiencies of nearly 80% were found near 3.0 GHz. As the frequency was increased towards the top end of the MSSW range, the coupling efficiency dropped off quite rapidly with insertion losses for the θ_2 position approaching the probe isolation values.

MSSW Parameter Identification

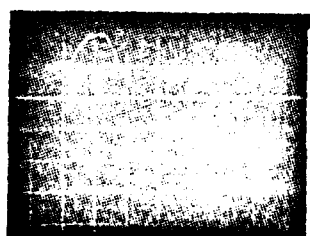
Using the group delay set-up shown in Figure 13, the group velocities at ring positions θ_1 and θ_2 were determined using 50 to 100 nanosecond wide pulses. The RF frequency was varied over a 2.8 to 3.2 GHz range. As seen in the sequence shown in Figure 16, the pulse delay increased with frequency. As the frequency approached the upper MSSW limit, pulse amplitude began to drop off abruptly. Distortion and pulse-spreading was also seen, but only at the very end of the MSSW frequency range. To insure that the pulse propagation mechanism was a surface wave phenomenon, a fine wire was



50 nanosecond delay
for θ_2 near 3.1 GHz.



100 nanosecond delay
for θ_2 near 3.16 GHz.



125 nanosecond delay
for θ_2 near 3.2 GHz.
Note large change in
amplitude and pulse
distortion.

Figure 16. Group Delay Sequence.

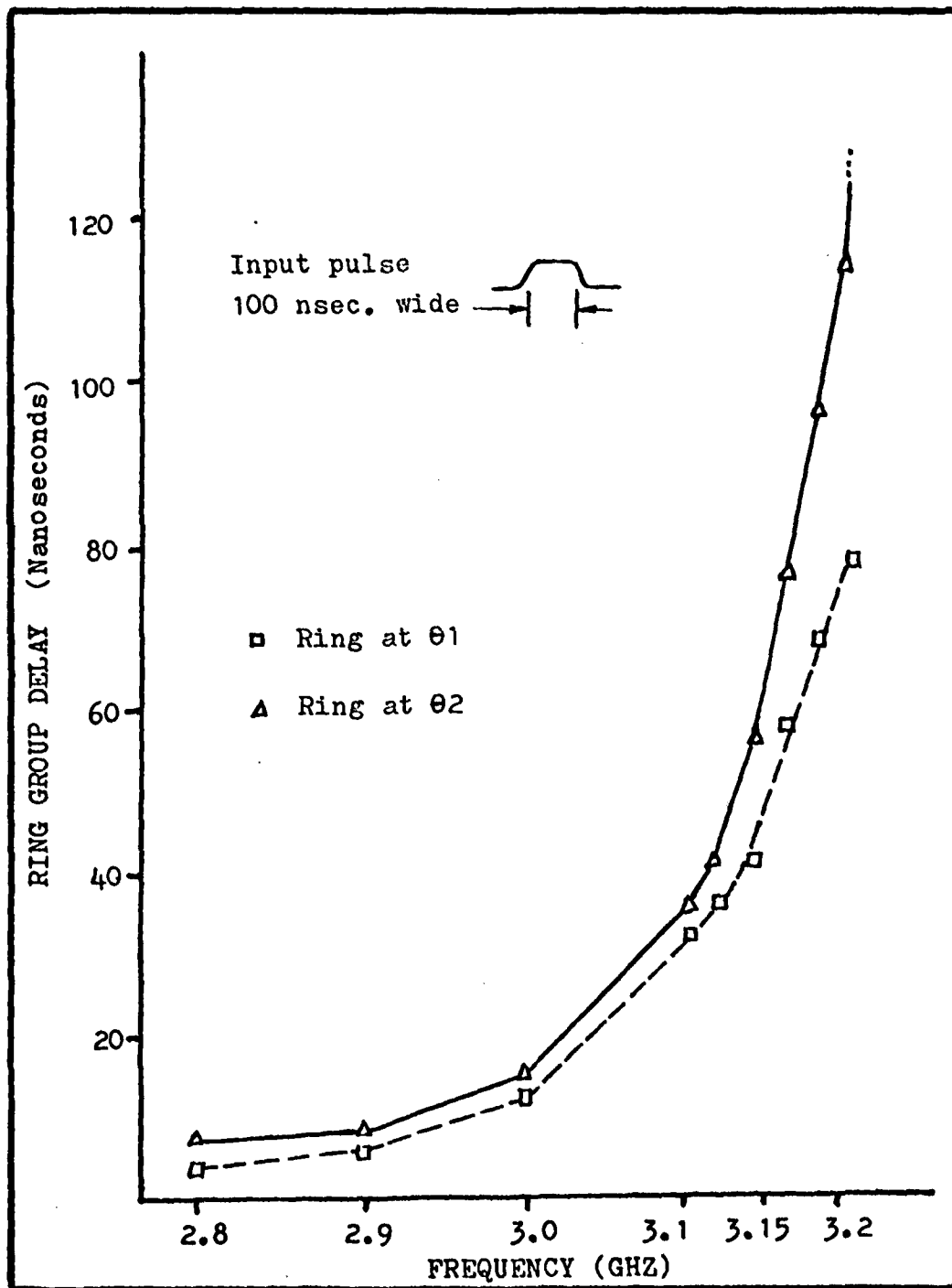


Figure 1 . Group Delay vs Frequency

TABLE V.

Measured and Calculated MSSW Parameters, θ_1

Freq. (GHz)	Group Delay (nsec)	Group Vel. (cm/ sec)	Effective k number (cm^{-1})	Effective Field, H_e (Oe.)	Effective Wavelength (cm)
2.80	4.0	500.0	4.84	231.	1.3
2.90	5.5	364.0	5.94	273.	1.06
3.00	12.0	166.7	8.86	233.	0.71
3.10	32.0	62.5	12.6	246.	0.50
3.12	36.0	55.6	13.0	252.	0.48
3.14	41.0	48.8	13.5	258.	0.47
3.16	58.0	34.5	14.8	262.	0.43
3.18	68.0	29.4	15.4	267.	0.41
3.20	78.0	25.6	15.9	274	0.40

TABLE VI.
Measured and Calculated MSSW Parameters, $\theta 2$

Freq. (GHz)	Group Delay (nsec)	Group Vel. (cm/ sec.)	Effective k number (cm^{-1})	Effective Field, H_e (Oe.)	Effective Wavelength (cm)
2.80	7.0	286.0	6.0	187.	1.05
2.90	8.0	250.0	7.4	249.	0.85
3.00	14.0	143.0	9.5	228.	0.66
3.10	36.0	55.6	13.0	245.	0.48
3.12	45.0	44.4	14.0	249.	0.45
3.14	56.0	35.7	15.0	255.	0.43
3.16	77.0	26.0	15.0	260.	0.40
3.18	96.0	20.8	17.0	266.	0.38
3.20	114.0	17.5	17.4	272.	0.36
3.20 ⁺	131. ⁺	15.3	18.0	272.	0.35

stretched across each of the two surface wave ring paths. For one surface path, the fine wire had no noticable effect. For the other surface, a decrease in the group delay was observed as was an increase in pulse amplitude. These results identified the magnetostatic surface wave propagation characteristics desired for the rotation rate experiments.

As previously noted, non-uniform behavior as a function of ring position was observed over the MSSW range. The same type of non-uniformity was also observed during the group delay experiments. For example, it was seen that the maximum delayed pulse at 3.2 GHz occurred at the θ_2 position. Minimum delay occurred at θ_1 . There was a forty-five percent variation in the θ_1 delay relative to the delay at θ_2 . This data is summarized in Tables V and VI and plotted in Figure 17.

Using this data and knowledge of the propagation path length, the effective wave number, k_e , can be determined as a dispersive function of frequency using

$$k_e = \frac{1}{2s} \ln \left[\frac{(4\pi M_s r)^2 s}{4\omega v_g} \right] \quad (39)$$

For Eqn (39), the group velocity is calculated by dividing the path length by the group delay. This effective

dispersion for the θ_1 and θ_2 positions is shown in Figure 18 where it is plotted against the theoretical dispersion calculated for the θ_2 position. This theoretical curve was produced by estimating the effective field, H_e , and noting its asymptotic value approaching the upper MSSW frequency limit. Eqn (30) then produced the final value based upon the group velocity that was actually measured.

The fact that there is a large displacement between the actual and theoretical θ_2 dispersions is believed to be a result of the flat slab assumption for the predicted dispersion model. For instance, it is interesting to note that the theoretical and actual curves do intersect as the k-numbers become very high. Indeed, the two curves level off at the same frequency asymptote. In this region, the surface waves are much smaller than the ring dimensions and the flat geometry assumption is satisfactory. Further improvement in the theoretical dispersion can be attained by using the following relation as formulated by Srivastava (Ref 15:254):

$$k' = k_s \left[\frac{s/R}{\ln(1 + s/R)} \right] > 1 \quad (40)$$

where k_s = the wave vector number based on a slab

k' = the corrected wave vector number based
on a cylindrical (ring) geometry.

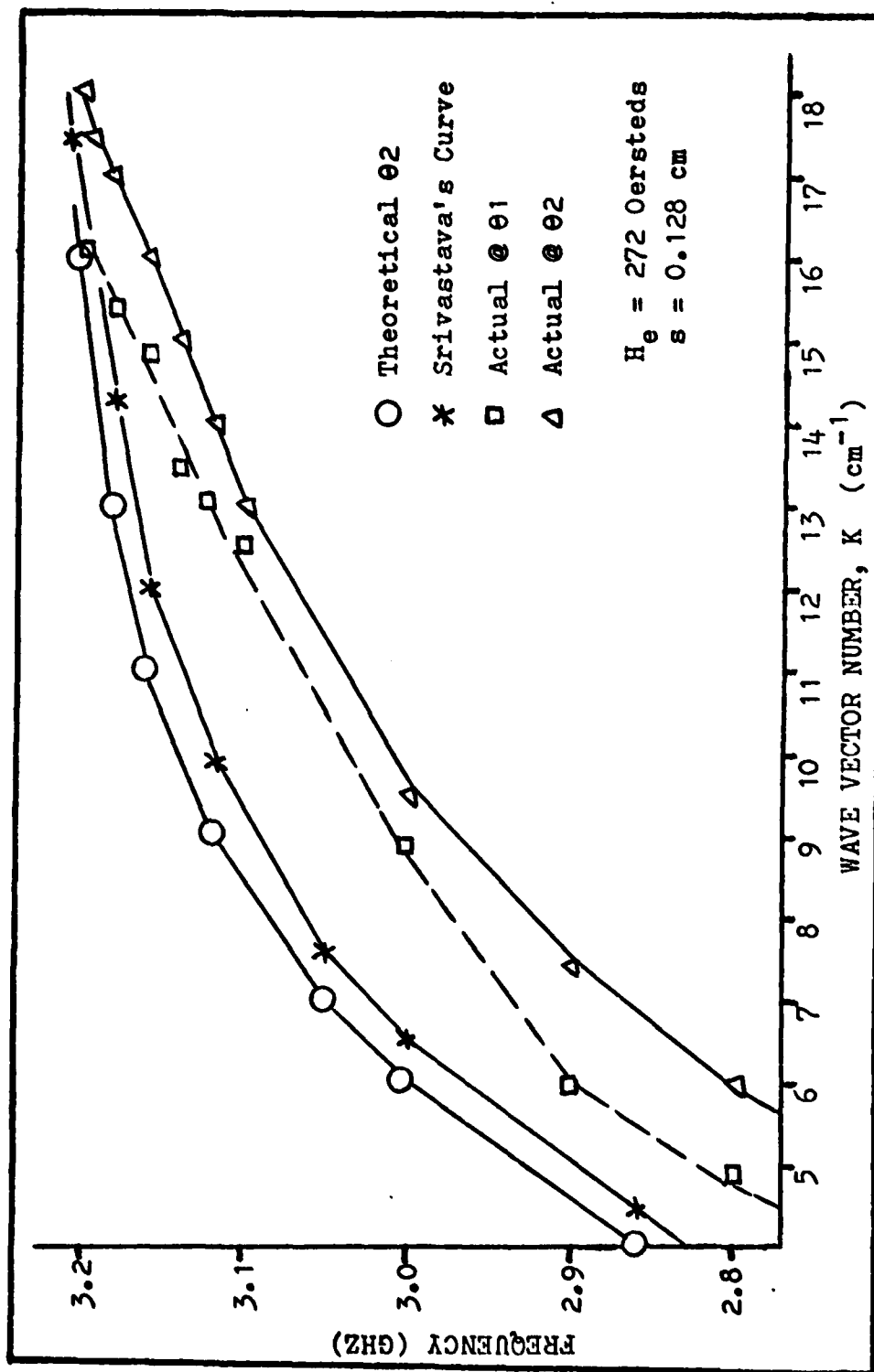


Figure 18. Comparative Dispersion Plots

Although the Srivastava plot in Figure 18 shows some improvement at the high frequencies for the cylindrical correction, the lower frequencies still remain displaced. It is postulated that this is a result of the induced MSSW wavelengths being fairly large compared to the ring. Under these circumstances, any correction to the dispersion relation must take into account the relationship of ring geometry to the propagating surface wavelengths. Several attempts were made to find a suitable topological correction, but without success. Despite this, the fact that the effective dispersion relation shifted in the direction predicted by Srivastava is an encouraging result (Ref 15:255). For the reader's convenience, the results of the parameter identification and loss measurements are summarized in Tables IV and V.

$\Delta\phi$ Experimental Results

As has been seen from both the system loss and group delay measurement data, non-uniform MSSW behavior was found as a function of the ring angular orientation relative to the probes. This obviously will have an effect on the performance of the $\Delta\phi$ rotation rate experiment. For example, using Eqn (16) and a phase velocity of 1118 cm/usec., a rotation rate of 3000 RPM yields a phase shift of 1.02 microradians. However, when this is

compared to a worst case variation in phase velocity due to the applied rotation rate will vary by ± 0.223 microradians or approximately twenty-two percent.

Although there are ways of handling this error, the more serious problem is the large variations in system insertion losses. At 3.2 GHz this was about 27 db as found by comparing the insertion losses at the θ_1 and θ_2 positions. If this is applied to the following expression which describes the system voltage output as a function of phase shift and ring position, the desired rate sensitivity is hopelessly swamped out by the large variations in system insertion losses:

$$\begin{aligned} E_o &= E_o'(\theta) \cos(\Delta\phi) \\ E_o'(\theta) &\gg E_o' \cos(\Delta\phi) \end{aligned} \quad (41)$$

where θ = discrete position of the ring

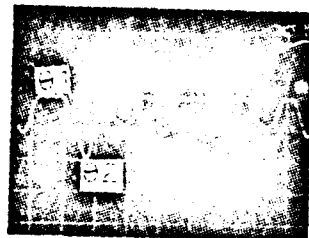
$\Delta\phi$ = phase shift due to applied rotation rate.

This effect can be seen in the photographic sequences in Figure 19. For three different rates, 1000, 2000, and 3000 RPM, the overall detected phase pattern remains essentially the same. Because of the periodicity of the coupling losses it is easy to determine the applied rotation rate frequency by measuring the time between

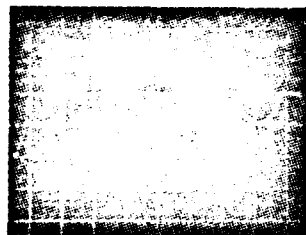
similar points on the repeating waveform. Also note that the θ_1 and θ_2 positions are marked on the photographs for reference. This conveniently illustrates the nearly 90° separation between θ_1 and θ_2 .

Another concern was how probe coupling and loading affected the MSSW modes on the ring (Ref 3). Figure 20 shows that there is little change in the phase pattern when the transmitting probe-to-ring distance was increased. The only noticeable change was the lessening of the detector saturation. This result eliminated coupling distance as a potential major source of distortion where ring eccentricity and wobble could have been important.

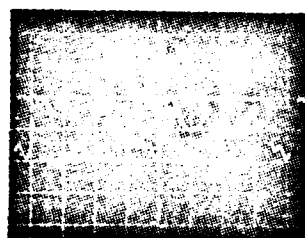
During the 4ϕ rate sensing experiment, several attempts were made to decipher and correlate the calculated scaling function, S_ϕ , with the recorded phase patterns. The loss variations, however, were so large that all attempts were unsuccessful. If smaller loss variations had been achievable, the problem of these large phase variations could have been reduced.



Phase pattern at
1000 RPM, 13.3 msec/div.



Phase pattern at
2000 RPM, 5 msec/div.



Phase pattern at
3000 RPM, 5 msec/div.

Upper level = 180°

Lower level = 0°

Figure 19. Sequence of Phase Patterns
at Different Rotation Rates

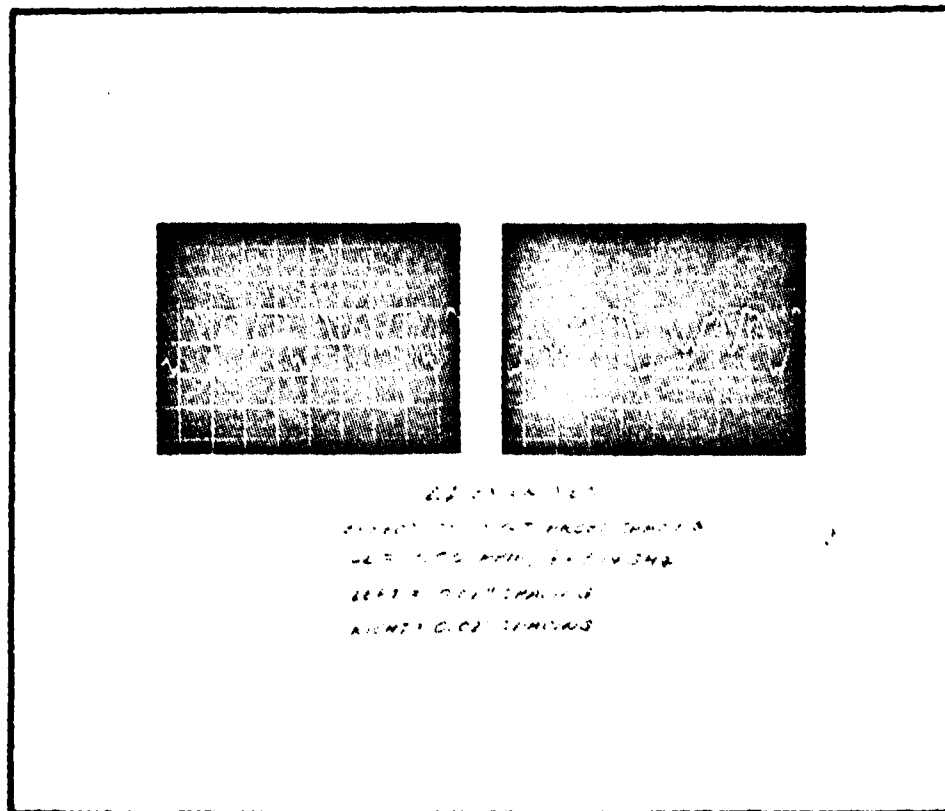


Figure 20. Phase Patterns as Influenced
by Coupling Distance.

THIS PAGE IS BEST QUALITY PRINT
 A COPY FURNISHED TO DDC

4f Experimental Results

Using the set-up shown in Figure 12, the variable phase shifter and oscillator loop attenuator were adjusted for stable oscillations. As previously demonstrated by Young (Ref 7), a comb of oscillator frequencies was generated as shown in Figure 21. For various loop adjustments, a wide range of frequencies were generated; however, the most stable appeared around 2.8 GHz.

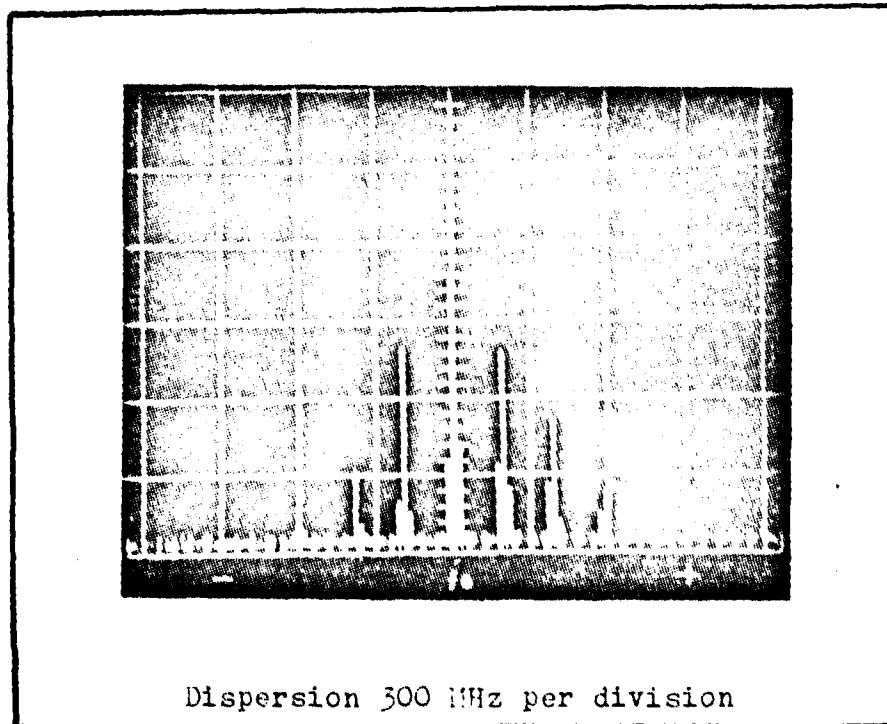
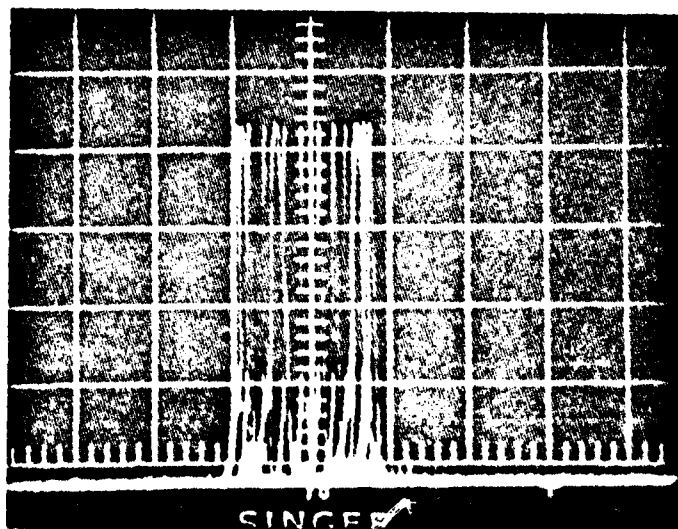


Figure 21. Comb Oscillator

Again referring to Figure 21, the difference in the comb frequencies is about 200 MHz which represents a net loop phase velocity of about 2500 cm/usec. This is somewhat slower than the phase velocity calculated from the group delay data; nonetheless, this value is reasonable considering the cumulative effect of measurement uncertainties and temperature drift.

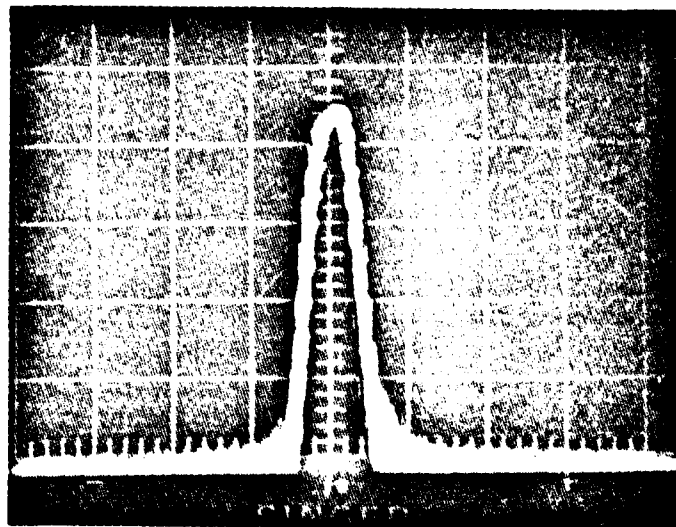
For rotation rate sensing, the double stub tuner was adjusted to yield a single oscillation frequency. When this condition was achieved for oscillations higher than 2.8 GHz, changes in the ring position resulted in frequency hopping to other lower, more stable modes. This was an undesirable condition; therefore, the oscillator stub tuner was readjusted along with the variable phase shifter to produce stable oscillations around 2.8 GHz. At this frequency, changes in ring position resulted in continuous shifts in the oscillator frequency. This effect is shown in Figure 22 where the ring was rotating at 3000 RPM. The net displacement of the oscillator frequency as measured with the spectrum analyzer was 1.8 MHz. This displacement was due to the non-uniform MSSW behavior which, as seen in previous experiments, was a function of ring orientation relative to the RF probes. Similar variations in the oscillator frequency like



Dispersion = 1MHz per div.
 $f_0 = 2.8 \text{ GHz}$ Applied 3000 RPM

Figure 22. Rotational Effects on MSSW
 Ring Oscillator Frequency

that shown in Figure 22 were artificially induced by varying the loop gain and phasing. This leads to the hypothesis that the actual displacement was a function of anisotropic losses and dispersion characteristics. In fact, calculated displacements due to changes in v_p indicated maximum displacements on the order of



Dispersion = 300 KHz per division
 Vertical log scale $f_o = 2.8$ GHz

Figure 23. MSSW Ring Oscillator Spectral Noise

700 MHz. This large of a displacement was not seen at 2.8 GHz. On the other hand, displacement due to a maximum rotation rate of 3000 RPM would be about 700 Hz. This small of a displacement was not detectable because of the large corruptive displacements and a signal noise bandwidth of approximately 100 KHz as seen in Figure 23.

Since the magnetic biasing field was originally allowed to rotate with the ring, the Δf set-up was next modified to keep the applied field fixed relative to the RF probes. This arrangement did not improve the variations in ring behavior due to positional changes. This would seem to further reenforce the hypothesis that anisotropic variations were accountable for the deviate loss and phase behavior. Ultimately, the ring fractured while being rotated at low RPM. The fracture seemed to follow a fine surface scar that was on the ring periphery. It is suspected that this was the site of a crystal plane dislocation owing to the features at the fracture. It is possible that either magnetic torques or shaft vibrations aggravated the dislocation and caused the final fracture.

Analysis of Corruptive Effects

As previously described, large variations in losses and dispersion were observed in all experiments as a function of the ring's orientation relative to the RF probes. At first these corruptive effects were thought to be the result of variations in the biasing field. Since the biasing field was allowed to rotate with the ring, it was speculated that the observed corruptive effects were simply manifestations of the launched surface

waves seeing different biasing conditions for incremental changes in the ring and bias field position. To eliminate this possibility, the experimental set-ups were modified to keep the biasing field stationary relative to the RF probes. Thus, all launched surface waves would be exposed to the same field conditions in their travel from the input to output probes. When the f experiment was performed with this change, the corruptive loss and dispersion effects remained essentially the same.

To further examine this result, a thin film YIG disc 10 microns thick on a GGG substrate was tested using the set-up shown in Figure 24. For this configuration the biasing field was held fixed relative to the probes and group delay and loss measurements were made. It was found that the thin film disc exhibited the same type of position-dependent behavior as the ring though not as severe. It is speculated that these variations are due to anisotropic effects which are dependent again on the crystal lattice orientation relative to the probes.

In reviewing the thick ring experiments where the biasing field rotated with the ring, the surface waves

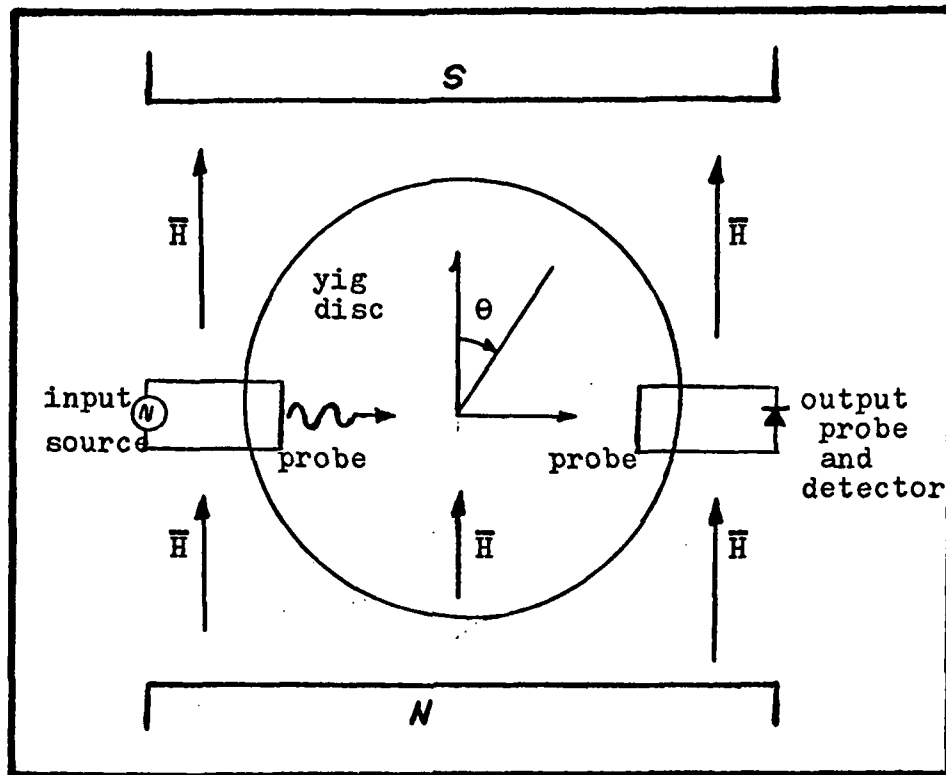


Figure 24. YIG Disc Set-Up to Observe Anisotropic Effects

were traveling at velocities much greater than the tangential velocity component due to the applied rotation rate; therefore, the bias field always looked relatively fixed compared to the propagating waves. For example, it is estimated that the shaft rotated 0.13 microradians for a rotation rate of 3000 RPM while the

MSSW travelled from the input to the output probe. It is suspected, however, that the crystal lattice and any anisotropic fields would be continuously changing at the mechanical rotation rate in the vicinity of the MSSW launch site. Consequently, the anisotropic field effects could have caused the corruptive behavior as seen during all experiments.

Experimental Summary

Based upon the results of the experiments performed, the following observations were made. First, the loss and dispersion variations are most likely attributed to crystalline defects and anisotropic characteristics. Conversely, any variations due to field inhomogeneity are ruled insignificant. Second, some of these effects seem to be independent of the YIG form, since similar behavior was observed on a high quality thin film YIG disc. Third, the large variations detected during group delay measurements prevented satisfactory detection of rotation rates for both the phase and frequency sensitive experiments. Fourth, the performance of the RF probes was very satisfactory with relatively efficient excitation and detection of the surface waves. Finally, for those cases where the MSSW wavelengths are large compared to the ring, further refinement of the dispersion relation is required to model the MSSW behavior.

VI. Conclusions

Summary

This thesis investigated the suitability of magnetostatic surface wave propagation around the periphery of the magnetically biased thick YIG ring to sense noninertial rotation rates. In one case, a phase sensitive interferometric rotation rate sensor was designed, built, and tested. In a second scheme, a frequency sensitive sensor was similarly investigated where shifts in the frequency of a MSSW ring oscillator provided rate information.

For both rate sensing schemes, large variations in the MSSW behavior around the ring prevented satisfactory rotation rate measurements. The non-uniform behavior was apparent in coupling loss and dispersion data that was initially measured during group delay measurements of the thick ring's MSSW parameters. Due to the large thickness of the YIG ring, the rotation rate scaling functions, S_θ and S_f , were very small since the thickness of the ring limited surface wave propagation to rather low wave vector numbers. The combined effect of low rate sensing sensitivities and non-uniform behavior due to suspected crystalline anisotropic fields made rotation

rate sensing impossible.

During group delay measurements of the ring MSSW parameters, it was seen that the effect of the ring curvature tended to shift the dispersion characteristics towards higher frequencies. This experimentally agreed with the prediction of Srivastava regarding MSSW propagation along curved ferrite surfaces. The experimental results suggest that additional modifications of the flat slab dispersion relation as used by Damon and Eshbach and Brundle and Freedman may also be required to account for the degree of curvature as compared to the propagating surface wave wavelengths.

For all experiments, an RF magnetic field probe design was proposed, tested, and used. The probe design has been shown to be capable of providing highly localized RF magnetic excitations while exhibiting up to 50 db isolation for probes slightly more than 0.5 inches apart.

Recommendations

In order to achieve higher rotation rate sensitivities, it is first recommended that the thickness of future YIG rings be limited to values much less than the thick ring used in this thesis. Since the thin film rings used by Sethares exhibited faceting as a consequence of the cubic crystalline structure of YIG, it is

recognized that this may still not be a satisfactory solution; however it is proposed that other thin film geometries such as a disc may be adapted to rotation rate sensing. This, however, requires the difficult task of designing a suitable radial magnetic biasing field.

It is also recommended that further study be devoted to the task of determining and modeling the observed non-uniform behavior of the YIG medium. It is suspected that this non-uniformity results from anisotropic fields that are very sensitive to the orientation of the crystal lattice relative to the surface wave launch site and propagation direction. Because of this effect, it is felt that any future investigation of MSSW rotation rate sensors be preceded by such an analysis.

Bibliography

1. Bongiani, W.L., et al. "Microwave Filters and Delay Lines," Technical Report AFAL-TR-73-72, April 1973.
2. Brundle, L.K., and Freedman, N.J. "Magnetostatic Surface Waves on a YIG Slab," Electronics Letters, 4:132-134 (April 1968).
3. ----- "Nonlinear Behavior of Magnetostatic Surface Waves," Electronics Letters, 4-20:427-428 (October 1968).
4. Damon, R.W., and Eshbach, J.R. "Magnetostatic Modes on a Ferromagnetic Slab," Journal of Phys. Chemical Solids, 31:308-320 (May 1960).
5. Kittel, C. Elementary Solid State Physics. John Wiley and Sons, New York, 1962.
6. ----- Introduction to Solid State Physics. John Wiley and Sons, New York, 1966.
7. Miller, N.D.J., and Brown, D. "Tunable MSSW Oscillator," Electronics Letters, 12-9:209-210 (April 1976).
8. Newburgh, R.G., Blacksmith, P., Budreau, A.J., and Sethares, J.C. "Acoustic and Magnetic Surface Wave Ring Interferometers for Rotation Rate Sensing," IEEE Proceedings: 62-12 (December 1974).
9. Roberts, J. High Frequency Application of Ferrites. D. Van Nostrand Co. Inc., Princeton, New Jersey, 19 .
10. Sethares, J.C. "Magnetostatic Surface Waves on a Cylinder," Technical Report AFCRL-TR-75-0830, 17 July 1975.
11. Sethares, J.C., and Merry, J.B. "Magnetostatic Surface Waves in Ferrimagnets Above 4 GHz," Technical Report AFCRL-TR-74-0112, 28 February 1974.
12. Sethares, J.C., and Stiglitz, M.R. "Propagation Loss and MSSW Delay Lines," IEEE Transactions on Magnetics, 10-3 (September 1974).

13. Soohoo, R.F. Theory and Application of Ferrites. Prentice-Hall, Inc., New Jersey, 1960.
14. Sparks, M. Ferromagnetic Relaxation Theory, McGraw-Hill, Inc., New York, 1964.
15. Srivastava, N.C. "Propagation of Magnetostatic Waves Along Curved Ferrite Surfaces," IEEE Transactions on Microwave Theory and Techniques, 26-4:252-256 (April 1978).
16. Von Aulock, W.H. Handbook of Microwave Ferrite Materials. Academic Press, Inc., New York, 1965.

AD-A080 372

AIR FORCE INST OF TECH WRIGHT-PATTERSON AFB OH SCH00--ETC F/6 20/3
ROTATION RATE SENSING VIA MAGNETOSTATIC SURFACE WAVE PROPAGATIO--ETC(U)
DEC 79 R J POTURALSKI

UNCLASSIFIED

AFIT/6E/EE/79-28

NL

2 of 2

NOV 20 1980

END

DATE

FILED

3-80

DOC

Appendix A: Symbols and Abbreviations

Symbol	Explanation
AFCRL	Air Force Cambridge Research Laboratories
AFIT	Air Force Institute of Technology
B	Magnetic flux density
d_p	RF probe diameter
E_o	Output voltage
f	Magnetostatic frequency
f_{lo}	Lowest magnetostatic frequency
f_{hi}	Highest magnetostatic frequency
G	Flux units, gauss
GGG	Gadolinium-Gallium-Garnet
H	Magnetic field intensity
H_a	Applied magnetic field
H_e	Effective or net internal field intensity
H_d	Demagnetizing field intensity
h_{rf}	RF field intensity
I_p	Probe isolation (in db)
k	Magnetostatic wave vector number
L	Propagation path length
\vec{M}	Magnetization vector
MSSW	Magnetostatic surface wave
MSVW	Magnetostatic volume wave
N_D	Demagnetization factor

Symbol	Explanation
\mathbf{n}	Surface normal unit vector
O_e	Field intensity units, Oersteds
P_i	System parameters, general
R	Ring radius
s	YIG sample thickness
S_f	Frequency sensitive scaling function
S_ϕ	Phase sensitive scaling function
t	Time
t_{delay}	Propagation group delay
T_1	Single spin system longitudinal component
T_2	Single spin system transverse component
v_g	Group velocity
v_p	Phase velocity
v_t	Tangential velocity component
γ	Gyromagnetic ratio
ΔH	YIG linewidth
Δf	Frequency shift
$\Delta \phi$	Phase shift
θ	Precession angle or ring displacement
λ	MSSW wavelength
τ	MSSW period
Ω	Applied rotation rate
ω	MSSW angular frequency
$4\pi M_s$	Saturation Magnetization

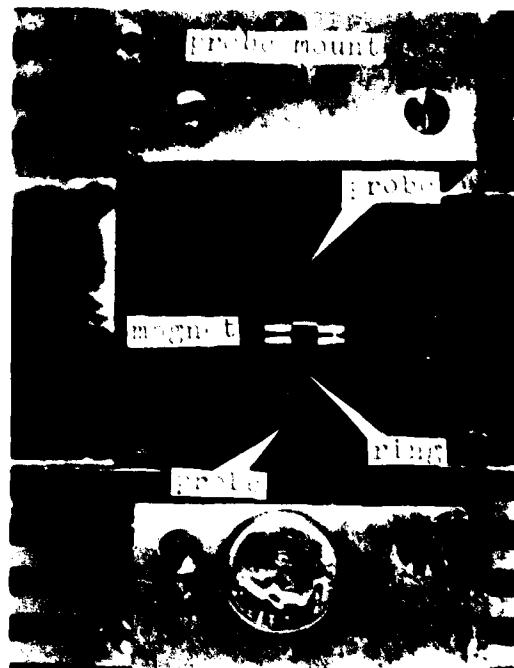
Appendix B: Equipment

The following is a list of the equipment used during the experimental phase of this thesis. Included in this section is a brief description of the equipment and identification of the manufacturer.

Equipment	Description
Microwave Source	RF generator, Hewlett-Packard, model TS-403/U. Tunable from 1.8 to 4.0 GHz. Maximum output is +3.0 dbm into 50 ohms.
Spectrum Analyzer	Alfred model MF-100 with model RF-3000 tuning head. Tunable from 0.01 to 40 GHz with adjustable dispersion from 1KHz to 300 MHz.
RF Power Meter	Hewlett-Packard HP 432A with model MT 478A thermistor mount. Seven ranges from 0.01 to 10 mw.
Oscilloscope	Tektronix model 465M dual input wideband oscilloscope. Fastest time base at 5 nsec (calibrated).
Microwave Amplifier	Varian traveling wave tube (TWT) model VTS-4413P1 with approximately 36 db gain over 2.0 to 4.0 GHz range. Low noise amplifier.

Motor and Controller	Electrocraft Corp. Motomatic controller and motor model E-650. Rates up to 3000 RPM cw. or ccw. Maximum torque of 5 in.-lb.
Video Amplifier	Keithly Instruments wideband video amplifier model 104. Choice of one megohm or 50 ohm inputs. Gains of 1, 10, or 100.
Pulse Generator	Hewlett-Packard model HP-8001A. Variable pulse width from 100 to 500 nanoseconds at repetition rates from 0.1 to 200 KHz. Maximum output of 10 volts into 50 ohms.
PIN Diode Modulator	Hewlett-Packard model 8732B. Frequency range from 1.8 to 4.5 GHz. Requires bias interface.
Lock-in Amplifier	Princeton Applied Research model NHR8. As tunable, filtered voltmeter and wave analyzer provides continuous tuning from 1.5 Hz to 150 KHz with meter time constant selections
Directional Coupler	Varian Associates model 3003-10 provides -10 db directional coupling over 2.0 to 4.0 GHz range.
RF Isolator	Microwave Associates model R439-353 provides over 20 db isolation over 2.0 to 4.0 GHz range.
Attenuator	Continuously adjustable uncalibrated attenuation. Antenna and Radome Research Associates model 3414-30 coaxial "PI" line attenuator.

Hybrid Tee	Narda coaxial hybrid tee model 3003 Provides 0 and 90 degree phase output/input connections, 2.0 to 4.0 GHz.
Circulator	Western Microwave Laboratory model CTS-2442, 2.0 to 4.0 GHz.
Adjustable Stubs	General Radio model 874-020 adjust- able 20 cm sectional line with stand and connectors. Two used to construct double stub tuner.
Detector	General purpose microwave tunable crystal detector equipped with 1N13 Sylvania crystal in HP mount.
RF Probe and Mount	Fabricated locally and used to excite surface waves via RF magnetic field excitations. Probe and mount shown in Figure 26 in this appendix. The complete set-up with the DC field biasing magnets is shown in Figure 25.
Thin Film Disc Mount	Fabricated locally, this piece of hard- ware consists of a cylindrical fixture with retainer to clamp the thin film disc into place. The back end of the fixture has a shaft which fits into the Motomatic equipment. See Figure 27 in this appendix.



RF probes are
at top and
bottom.

Rotating shaft
runs horizont-
ally from left
to right.

Bias magnets
are left and
right of center

Ring is at
center of the
photograph.

Figure 25. RF Probe and Ring
Assembly

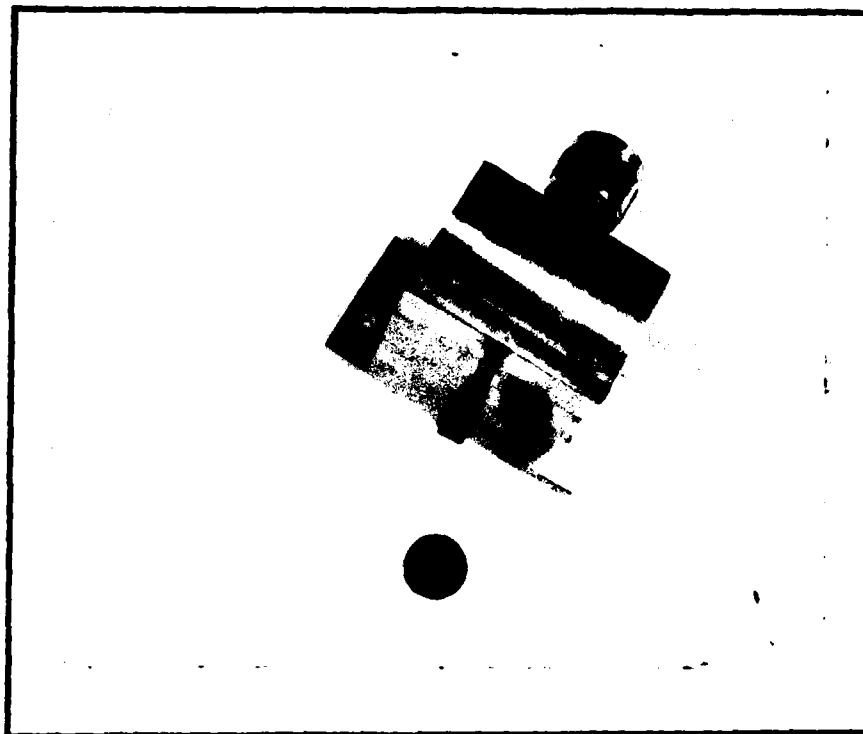


Figure 26. RF Probe and Mount

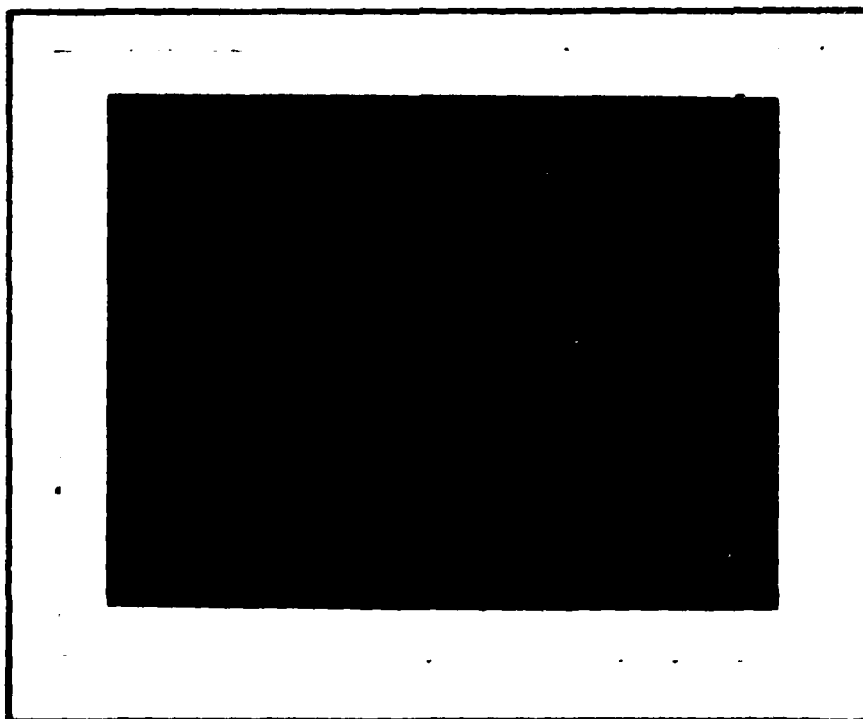


Figure 27. Thin Film Disc Mount

VITA

Richard J. Poturalski was born on 2 December 1945 in Baltimore, Maryland. After graduating from Baltimore Polytechnic Institute in 1963, he attended Baltimore Community College and the Johns Hopkins University in Baltimore. In 1968, he enlisted in the Air Force and later completed his degree work under the Airmen Commissioning and Education Program at Auburn University. He graduated with his bachelor of science degree in electrical engineering in June, 1973, cum laude. After commissioning in September, 1973, he was assigned to the Air Force Satellite Control Facility in Sunnyvale, California where he served both as electrical engineer and project manager within the Directorate of Planning and Development. In June, 1978, he entered the Air Force Institute of Technology where his studies will lead to a master of science degree in electrical engineering specializing in avionic control and guidance systems.

Permanent Address: 238 S. East Avenue
Baltimore, MD 21224

UNCLASSIFIED

SECURITY CLASSIFICATION OF THIS PAGE (When Data Entered)

REPORT DOCUMENTATION PAGE		READ INSTRUCTIONS BEFORE COMPLETING FORM
1. REPORT NUMBER AFIT/GE/EE/79-28	2. GOVT ACCESSION NO.	3. RECIPIENT'S CATALOG NUMBER
4. TITLE (and Subtitle) Rotation Rate Sensing via Magnetostatic Surface Wave Propagation on a Thick YIG Ring		5. TYPE OF REPORT & PERIOD COVERED MS Thesis
7. AUTHOR(s) Richard J. Poturalski Captain USAF		6. PERFORMING ORG. REPORT NUMBER
9. PERFORMING ORGANIZATION NAME AND ADDRESS Air Force Institute of Technology (AFIT/ENA) Wright-Patterson AFB, Ohio 45433		8. CONTRACT OR GRANT NUMBER(s)
11. CONTROLLING OFFICE NAME AND ADDRESS RADC/EEA Hanscom AFB, Massachusetts 01731		10. PROGRAM ELEMENT, PROJECT, TASK AREA & WORK UNIT NUMBERS
12. REPORT DATE December 1979		13. NUMBER OF PAGES 90
14. MONITORING AGENCY NAME & ADDRESS (if different from Controlling Office)		15. SECURITY CLASS. (of this report) Unclassified
		15a. DECLASSIFICATION DOWNGRADING SCHEDULE
16. DISTRIBUTION STATEMENT (of this Report) Approved for public release; distribution unlimited.		
17. DISTRIBUTION STATEMENT (of the abstract entered in Block 20, if different from Report)		
18. SUPPLEMENTARY NOTES Approved for Public Release; IAW AFR 190-16 Major Joseph C. Hipps Director of Public Affairs		
19. KEY WORDS (Continue on reverse side if necessary and identify by block number) Rotation Rate Sensing Magnetostatic Surface Waves Yttrium-Iron-Garnet		
20. ABSTRACT (Continue on reverse side if necessary and identify by block number) This thesis investigates the feasibility of using a thick (0.13 cm) yttrium-iron-garnet (YIG) ring to support magnetostatic surface waves for sensing noninertial rotation rates. Two rotation rate sensor designs are explored along with analysis of the actual YIG ring performance versus the standard slab geometry. Loss, group delay, and dispersion data are provided along with an analysis of observed corruptive effects. The investigation includes a brief study of a thin film YIG disc's performance compared to the YIG ring.		